PAPER

Convex blind image deconvolution with inverse filtering

View the article online for updates and enhancements.

Convex blind image deconvolution with inverse filtering

Xiao-Guang Lv[1], Fang Li[2] and Tieyong Zeng[3]

[1] School of Science, Huaihai Institute of Technology, Lianyungang, Jiangsu, People's Republic of China
[2] Department of Mathematics, East China Normal University, Shanghai, People's Republic of China
[3] Department of Mathematics, The Chinese University of Hong Kong, Shatin, Hong Kong

E-mail: zeng@math.cuhk.edu.hk

Abstract

Blind image deconvolution is the process of estimating both the original image and the blur kernel from the degraded image with only partial or no information about degradation and the imaging system. It is a bilinear ill-posed inverse problem corresponding to the direct problem of convolution. Regularization methods are used to handle the ill-posedness of blind deconvolution and get meaningful solutions. In this paper, we investigate a convex regularized inverse filtering method for blind deconvolution of images. We assume that the support region of the blur object is known, as has been done in a few existing works. By studying the inverse filters of signal and image restoration problems, we observe the oscillation structure of the inverse filters. Inspired by the oscillation structure of the inverse filters, we propose to use the star norm to regularize the inverse filter. Meanwhile, we use the total variation to regularize the resulting image obtained by convolving the inverse filter with the degraded image. The proposed minimization model is shown to be convex. We employ the first-order primal-dual method for the solution of the proposed minimization model. Numerical examples for blind image restoration are given to show that the proposed method outperforms some existing methods in terms of peak signal-to-noise ratio (PSNR), structural similarity (SSIM), visual quality and time consumption.

Keywords: blind image deconvolution, total variation, star norm, primal-dual, regularization

(Some figures may appear in colour only in the online journal)

1. Introduction

The recorded images are often degraded by blur and additive noise due to environmental effects and imperfections in the imaging system. In the image capturing process, blurring usually occurs due to out-of-focus lens, atmosphere turbulence, relative movement between scene and camera or object motion during exposure time (Banham and Katsaggelos 1997, Vogel 2002, Hansen *et al* 2006, Bonettini *et al* 2008, Katsevich *et al* 2011, Borcea *et al* 2013, Lou *et al* 2014). Blurring causes spread of edges, which leads to the loss of sharpness and contrast in the recorded image. Noise is an undesirable by-product of image recording that adds spurious and extraneous information. Image restoration is the task of estimating the original image from blurred and noisy measurements. Mathematically, a space-invariant model for the degraded image is expressed as a convolution of an original image and a point spread function (PSF), plus the Gaussian noise (Jiang and Wang 2003, Calvetti *et al* 2004, Chan and Shen 2005, Fornasier *et al* 2012):

$$g = h * f + \eta, \tag{1}$$

where $*$ denotes the two-dimensional linear convolution operator, g is the degraded image, f is the original image, η is the additive Gaussian noise and h is a PSF which represents the linear shift-invariant blur kernel. If the blur kernel is given as a prior, estimating the original image is known as a nonblind deconvolution problem. In the past, the nonblind deconvolution algorithms such as Tikhonov regularization, total variation (TV) regularization and wavelet frame regularization have been proposed (Tikhonov and Arsenin 1977, Rudin *et al* 1992, Abdoulaev *et al* 2005, Paragios *et al* 2006, Dong *et al* 2011, Ito and Jin 2011, Cai *et al* 2012a, Chan *et al* 2013, Gerth and Ramlau 2014, Pöschl and Scherzer 2015, Bao *et al* 2016).

However, the blur kernel of the degraded model is usually unknown in most real applications such as astronomical imaging, remote sensing, microscopy, medical imaging, optics, photography, super-resolution and motion tracking applications. Such estimation problems are often called blind deconvolution. In blind deconvolution, we need to simultaneously estimate the blur kernel h and recover the original image f directly from the degraded image g with only partial or no information about degradation and the imaging system (Justen and Ramlau 2009, Zunino *et al* 2009, Campisi and Egiazarian 2016). The major difficulty experienced in blind deconvolution lies in the insufficient information of two unknown variables and the existence of the additive noise. This poses problems in the process of image restoration when there may be many or even possibly an infinite number of unmeaningful solutions.

For the past decades, a lot of research has been done to develop fast and robust algorithms for handling the ill-posedness of blind deconvolution. Generally, there are three main classes of methods for blind deconvolution of images. The first class is a two-step approach. It identifies the PSF in the first step and then use it to recover the original image with one of the conventional image restoration methods in the second step. To achieve successful restoration, it is important to estimate the PSF as accurately as possible. The major advantage of this class is the low computational complexity. The drawback is that they can be used only in the case that the true image and the PSF are known to have special characteristics (Joshi *et al* 2008, Xu and Jia 2010). The second class is more generally applicable, which recovers the original image and estimates the PSF simultaneously. This class can be further divided into parametric and nonparametric methods. The parametric methods assume that the original image or the PSF follows some model. Popular parametric models include the PSFs resulting from a Gaussian blur system, an autoregressive prior system, linear camera motion and out-of-focus lens system (Molina and Ripley 1993, Kundur and Hatzinakos 1996, Likas and Galatsanos 2004, Chung and Nagy 2010). The nonparametric estimation approaches do not assume any

parametric model of the original image or the PSF. Instead, they utilize deterministic constraints on the PSF or the original image such as nonnegativity, known finite support and existence of invariant edges. One of the earliest nonparametric methods is the iterative blind deconvolution (IBD) algorithm developed by Ayers and Dainty (1988). In the IBD method, it is assumed that the PSF is nonnegative with known finite support constraint. The IBD method is widely used due to its low computational complexity and its robustness in the presence of additive noise. The major disadvantage of the IBD method is that the global convergence has not been proved. Another nonparametric method given by McCallum (1990) estimates the PSF and the original image by minimizing a multimodal cost function with a simulated annealing (SA) algorithm. The SA method is reliable and produces reasonable results in the presence of noise. But the slow convergence and high computational complexity are major obstacles limiting the real-time applications. Later, nonparametric methods based on regularizers for both the original image and the PSF are proposed to handle the bilinear ill-posedness of blind deconvolution. In Chan and Wong (1998), Chan and Wong proposed double TV regularizers for blind deconvolution of images. The motivation for using TV regularization for both the PSF and the original image is due to the fact that the PSF and the original image usually have edges. Numerical results indicate that the double TV scheme is quite robust to noise especially for discontinuous blur. To greatly reduce the computational cost and improve the image quality, the split Bregman iteration approach was employed in Li *et al* (2012) for solving the double TV blind deconvolution model. Recently, a nonparametric regularization approach was proposed in Cai *et al* (2012b) to remove a motion blurred image due to camera shake by regularizing the sparsity of both the original image and the motion blur kernel under tight wavelet frame systems. The authors used an adapted version of the split Bregman method to efficiently solve the resulting minimization problem. The third class of blind deconvolution is the inverse filtering methods. Approaches which belong to this class estimate the inverse of the PSF and then obtain the approximate image of the original image by convolving the degraded image with the inverse filter. One of the most popular inverse filtering method is the nonnegativity and support constraints recursive inverse filtering (NAS-RIF) algorithm proposed by Kundur and Hatzinakos (1998). The NAS-RIF method imposes the nonnegativity and known finite support constraint on the original image, and assumes that the PSF and its inverse are absolutely summable. A variable finite impulse response (FIR) inverse filter was used to convolve with the degraded image and the resulting output is an estimate of the original image. The major advantage of the NAS-RIF method is that it has lower computational complexity level and fast convergence to a feasible set of solutions. However, numerical simulations show that the NAS-RIF method is very sensitive to noise due to the high pass property of the inverse filter which amplifies high frequency noise. As a result, the converged solution may not be the best estimate of the original image in the presence of noise. Although Kundur and Hatzinakos suggested that the noise amplification problem can be relieved by terminating the restoration procedure through visual inspection, in practice, it has never been easy to determine which is the optimal iteration for termination. In order to reduce noise amplification, a regularization proposed by Ng *et al* (2000) is applied for the inverse filter used in the NAS-RIF method. At each iteration, the eigenvalues of the convolution matrix corresponding to the inverse filter, which are below a threshold are suppressed and the resulting error is also made a part of the overall objective function. Preliminary numerical results on some simulated and optical imaging problems indicate the effectiveness of the method. Other inverse filtering methods and extension of the NAS-RIF method can be found in Benameur *et al* (2008), Dolui and Michailovich (2011), Matsuyama *et al* (2000), Michailovich and Tannenbaum (2007), Ong and Chambers (1999) and Wang and Ng (2016).

In this paper, we investigate a regularized inverse filtering method for blind deconvolution of images. In the proposed method, two regularization terms are added to the objective function of NAS-RIF so as to improve the quality of blind image restoration. One regularization term is the total variation of the resulting image, which is obtained by convolving the inverse filter with the degraded image. The TV regularization from Rudin *et al* (1992) is used to stabilize the inverse solution and alleviate the sensitivity to noise. Especially, the TV regularization method is effective in preserving sharp edges without penalizing smooth regions. Another regularization term is the star norm (Vese and Osher 2003, Aujol *et al* 2005) of the inverse filter. For the prior of the inverse filter, we choose the star norm as the regularization function. The reason is that the inverse filter lies in a space which contains signals with large oscillations such as textures and has a small norm in this space. We show that the proposed minimization model is convex. The first-order primal-dual method from Chambolle and Pock (2011) is applied to compute the solution of the proposed minimization problem. Quantitative and qualitative experimental evaluations demonstrate that the proposed method performs better than some existing related restoration methods.

The rest of this paper is outlined as follows. In section 2, we discuss the properties of the inverse filters. In section 3, we propose a novel minimization model for blind deconvolution of images and analyze the convexity of the proposed minimization model. In section 4, we first briefly introduce the first-order primal-dual algorithm, and then employ it to compute the solution of the proposed minimization problem. Section 5 is devoted to illustrating the performance of the proposed approach. We give the concluding remarks in section 6.

2. The basic properties of inverse filters

In this section, we study the oscillation and symmetric properties of the inverse filters. Let us first consider the signal/image degradation model (1) without noise:

$$g = h * f.$$

In order to recover the true signal/image f, we need to find the inverse filter u of h, such that

$$f = u * g. \tag{2}$$

2.1. 1D inverse filter

To better understand the inverse filters, we begin with the one-dimensional discrete deconvolution problem. Let the original signal be

$$\hat{f} = (f_{-l+1}, \ldots, f_0, f_1, \ldots, f_n, f_{n+1}, \ldots, f_{n+l})^T$$

and the PSF be given by

$$h = (h_{-l}, h_{-l+1}, \ldots, h_0, h_1, \ldots, h_{l-1}, h_l)^T$$

with center h_0 and $\sum_{j=-l}^{l} h_j = 1$. The convolution of h and $\hat{f}$ leads to the blurred signal g, with $g_i = \sum_{j=i-l}^{i+l} h_{i-j} f_j$. In the matrix form (Ng *et al* 1999, Lv *et al* 2012), we have

$$
\begin{pmatrix} g_1 \\ \vdots \\ g_n \end{pmatrix} = \begin{pmatrix} h_l & \cdots & h_0 & \cdots & h_{-l} & & & & \\ & h_l & \ddots & h_0 & \cdots & h_{-l} & & 0 & \\ & & \ddots & \ddots & \ddots & \ddots & \ddots & & \\ & & & \ddots & \ddots & \ddots & \ddots & \ddots & \\ & 0 & & & h_l & \cdots & h_0 & \cdots & h_{-l} \\ & & & & & h_l & \cdots & h_0 & \cdots & h_{-l} \end{pmatrix} \begin{pmatrix} f_{-l+1} \\ f_{-l+2} \\ \vdots \\ f_0 \\ f_1 \\ \vdots \\ f_n \\ f_{n+1} \\ \vdots \\ f_{n+l-1} \\ f_{n+l} \end{pmatrix}. \tag{3}
$$

The purpose of the nonblind signal restoration is to recover the vector $f = (f_1, \cdots, f_n)^T$ given the PSF h and the blurred signal $g = (g_1, \cdots, g_n)^T$. Thus the blurred signal g is determined not only by f, but also by the boundary conditions $(f_{-l+1}, \ldots, f_0)^T$ and $(f_{n+1}, \ldots, f_{n+l})^T$. In this paper, we use the periodic boundary conditions (BCs). For this case, the data outside f satisfies

$$
\begin{cases} f_0 = f_n \\ \vdots \\ f_{-l+1} = f_{n-l+1} \end{cases} \quad \text{and} \quad \begin{cases} f_{n+1} = f_1 \\ \vdots \\ f_{n+l} = f_l \end{cases}.
$$

By straightforward computation and careful arrangement, it is not difficult to know that (3) can be rewritten as

$$
Hf = g,
$$

where H is an $n \times n$ circulant matrix given by

$$
H = \begin{bmatrix} h_0 & \cdots & h_{-l} & & & 0 \\ \vdots & \ddots & \ddots & \ddots & & \\ h_l & \ddots & \ddots & \ddots & \ddots & \\ & \ddots & \ddots & \ddots & \ddots & h_{-l} \\ & & \ddots & \ddots & \ddots & \vdots \\ 0 & & & h_l & \cdots & h_0 \end{bmatrix} + \begin{bmatrix} 0 & & & h_l & \cdots & h_1 \\ & & & & \ddots & \vdots \\ & & & & & h_l \\ h_{-l} & & & & & \\ \vdots & \ddots & & & & \\ h_{-1} & \cdots & h_{-l} & & & 0 \end{bmatrix}.
$$

It should be noted that the $(\left[\frac{n}{2}\right] + 1)$th column of the circulant matrix H is $h_{\text{big}} = [0, \ldots, 0, h, 0, \ldots, 0]^T$ with $\left[\frac{n}{2}\right] - l$ zeros before h, where $\left[\frac{n}{2}\right]$ is the largest integer not exceeding $\frac{n}{2}$. It is straightforward that $h * f = h_{\text{big}} * f = f * h_{\text{big}} = g$.

Let $\omega = e^{-i\frac{2\pi}{n}}$ and $i^2 = -1$ throughout the paper. In the following proposition, we give the existence and uniqueness of the inverse filter in the one-dimensional case.

Proposition 2.1. *For each interger $n \geqslant 2l + 1$, there exists a unique inverse filter u of h in (3) if and only if $\prod_{j=1}^{n} \varphi(\omega^{j-1}) \neq 0$ where $\varphi(x) = \sum_{j=-l}^{l} h_j x^j$. Moreover, the inverse filter u is given by the $(\left[\frac{n}{2}\right] + 1)$th column of the inverse matrix of H.*

Proof. It is well-known that any circulant matrix can be diagonalized by the Fourier transformation matrix (Ng 2004, Lv *et al* 2009). For the circulant matrix H, we have

$$H = F^*\Lambda F,$$

where F^* is the conjugate transpose of F and F is the n-by-n Fourier transformation matrix whose entries are given by

$$(F)_{jk} = \frac{1}{\sqrt{n}}e^{-i\frac{2\pi(j-1)(k-1)}{n}}, \quad 1\leqslant j,k\leqslant n$$

Here, $\Lambda = \mathrm{diag}(\lambda_1,\ldots,\lambda_n)$ is a diagonal matrix where λ_j is the jth eigenvalue of H. We may immediately obtain that $\lambda_j = \varphi(\omega_{j-1})$. If $\prod_{j=1}^{n}\varphi(\omega_{j-1}) \neq 0$, the matrix H is invertible and the inverse matrix H^{-1} is unique. Similar as the construction of H from h, we can get the inverse filter u from H^{-1} by extracting the $([\frac{n}{2}]+1)$th column. $\qquad\square$

Let F_j be the jth row of the Fourier transformation matrix F. We can write H as

$$H = \sum_{j=1}^{n}\lambda_j F_j^* F_j.$$

If H is nonsingular, we have

$$H^{-1} = \sum_{i=1}^{n}\lambda_j^{-1} F_j^* F_j.$$

Note that $F_j^* F_j, j = 1,\ldots,n$ can be seen as basis matrices for H and H^{-1}. As the value $|\lambda_j|$ decreases, the real part and the imaginary part of the basis matrix $F_j^* F_j$ tend to have more oscillations. See (Hansen *et al* 2006, chapter 5) for more details.

For example, let $h = [0.25,0.5,0.25]^T$ and $n = 15$. To illustrate the oscillation structure, we display signs of the real part and the imaginary part of the basis matrix $F_j^* F_j$ for $j = 1,\cdots,15$ in figures 1(a) and (b). It can be seen that as the index j increases from 1 to 8 and decreases from 15 to 9, the basis matrix tends to have more high frequency content, ranging from the flat appearance to matrices with more oscillations. We plot $|\lambda_j|$ in figure 1(c). Note that if n is odd, then λ_j and λ_{n-j+2} are conjugate pairs for $j = 2,\ldots,\frac{n+1}{2}$ and $\lambda_1 \in \mathbb{R}$. It is clear in figure 1 that the smaller $|\lambda_j|$ is, the more oscillations the basis matrix $F_j^* F_j$ has. In this example, the basis matrices $F_8^* F_8$ and $F_9^* F_9$ have the largest oscillations. In figure 1(d), we plot the absolute value of eigenvalues $|\lambda_j^{-1}|$ for the inverse matrix. It is obvious that the basis matrix $F_j^* F_j$ corresponding to the smaller value $|\lambda_j|$ contributes much more to H^{-1}. Hence, H^{-1} has oscillations. Due to the circulant structure of H^{-1}, the inverse filter u (the $([\frac{n}{2}]+1)$th column of H^{-1}) also has oscillations. We show the signs of H^{-1} in figure 1(e). In figure 1(f), we plot the signs of the inverse filter u, which is the 8th column of H^{-1}. We see from this figure that the inverse filter has oscillations.

2.2. 2D inverse filter

The results of the one-dimensional discrete problems can be extended in a natural way to two-dimensional discrete image deconvolution problems. Let the original image be $f = (f_{jk})_{j,k=1}^{m,n} \in \mathbb{R}^{m\times n}$ and the PSF be $h = (h_{jk})_{j,k=-l}^{l} \in \mathbb{R}^{(2l+1)\times(2l+1)}$ with center $h_{0,0}$ and $\sum_{j,k=-l}^{l}h_{j,k} = 1$. With the periodic BCs, the resulting blurring matrix H is a block circulant matrix with circulant blocks. We extend the dimension of h by padding with zeros
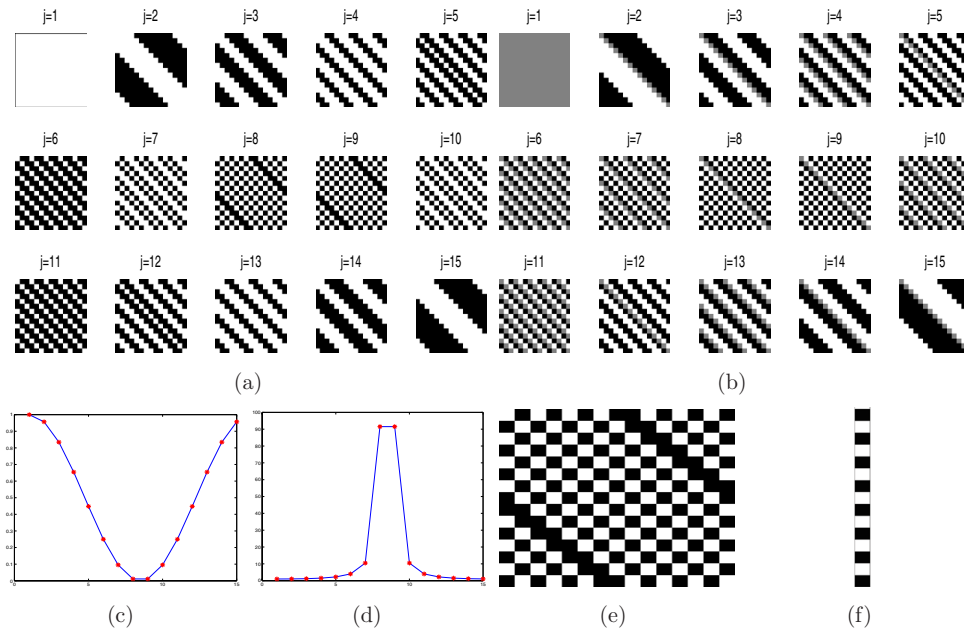
Figure 1. 1D example: $h = [0.25, 0.5, 0.25]^T$, $n = 15$. (a) Signs of the real parts of the basis matrices (size: 15×15); (b) signs of the imaginary parts of the basis matrices (size: 15×15); (c) the absolute value of eigenvalues for H; (d) the absolute value of eigenvalues for the inverse matrix H^{-1}; (e) signs of the inverse matrix (size: 15×15); (f) signs of the inverse filter(size: 15×1). (In (a), (b), (e) and (f), white: positive elements, black: negative elements, gray: zero elements).

to obtain the big PSF so that it has the same dimension as the original image. Let the m-by-n big PSF h_{big} be given by

$$h_{\text{big}} = \begin{pmatrix} 0 & 0 & 0 \\ 0 & h & 0 \\ 0 & 0 & 0 \end{pmatrix}$$

where the upper left corner is the $(\lceil \frac{m}{2} \rceil - l) \times (\lceil \frac{n}{2} \rceil - l)$ zero matrix. The blurring matrix H can be constructed from the big PSF. We stack all the elements of h_{big} along columns and put the resulting vector at the $(\lceil \frac{n}{2} \rceil m + \lceil \frac{m}{2} \rceil + 1)$th column of H. Then we obtain all elements of H using the block circulant with circulant blocks structure.

Proposition 2.2. *For each interger $m, n \geqslant 2l + 1$, there exists a unique inverse filter u of h if and only if $\prod_{j,k=1}^{m,n} \varphi(\omega^{j-1}, \omega^{k-1}) \neq 0$ where $\varphi(x, y) = \sum_{j,k=-l}^{l} h_{j,k} x^j y^k$. Moreover, the inverse filter u is obtained by reshaping the $(\lceil \frac{n}{2} \rceil m + \lceil \frac{m}{2} \rceil + 1)$th column of the inverse matrix of H into an $m \times n$ array.*

Proof. It is shown in Hansen *et al* (2006) that the block circulant matrix H with circulant blocks has the following spectral decomposition

$$H = F^* \Lambda F,$$

where $F = E_n \otimes E_m$, E_j ($j = m, n$) is the j-by-j Fourier transformation matrix and $\otimes$ denotes the Kronecker product operator, Λ is a diagonal matrix whose diagonal elements

are the eigenvalues of H. Since $FH = \Lambda F$, we have $\Lambda e_{mn} = E_n \otimes E_m H I_1$ where e_{mn} is the mn-dimensional vector of all ones and $I_1 = (1, 0, \ldots, 0)^T$. Hence, the eigenvalues of H can be obtained by the two-dimensional discrete Fourier transformation of the first column of H. Let λ_{jk} be the $(km - m + j)$th eigenvalue of H. We obtain that $\lambda_{jk} = (E_m H_{m,n} E_n)_{j,k}$ for $j = 1, \ldots, m$ and $k = 1, \ldots, n$, where $H_{m,n}$ is obtained by reshaping the first column of H into an $m \times n$ matrix. More precisely, we have

$$
H_{m,n} = \begin{pmatrix}
h_{0,0} & h_{0,1} & \cdots & h_{0,l} & 0 & h_{0,-l} & \cdots & h_{0,-1} \\
h_{1,0} & h_{1,1} & \cdots & h_{1,l} & 0 & h_{1,-l} & \cdots & h_{1,-1} \\
\vdots & \vdots & \cdots & \vdots & 0 & 0 & \vdots & \vdots \\
h_{l,0} & h_{l,1} & \cdots & h_{l,l} & 0 & h_{l,-l} & \cdots & h_{l,-1} \\
0 & 0 & \cdots & 0 & \vdots & 0 & \cdots & 0 \\
h_{-l,0} & h_{-l,1} & \cdots & h_{-l,l} & 0 & h_{-l,-l} & \cdots & h_{-l,-1} \\
\vdots & \vdots & \cdots & \vdots & \vdots & \vdots & \cdots & \vdots \\
h_{-1,0} & h_{-1,1} & \cdots & h_{-1,l} & 0 & h_{-1,-l} & \cdots & h_{-1,-1}
\end{pmatrix}.
$$

It then follows that $\lambda_{jk} = \varphi(\omega^{j-1}, \omega^{k-1})$ with $\varphi(x, y) = \sum_{j,k = -l}^{l} h_{j,k} x^j y^k$. If $\prod_{j,k = 1}^{m,n} \varphi(\omega^{j-1}, \omega^{k-1}) \neq 0$, the matrix H is invertible and the inverse matrix H^{-1} is unique. Similar as the construction of the block circulant with circulant blocks matrix H, we can get the inverse filter u by reshaping the $([\frac{n}{2}]m + [\frac{m}{2}] + 1)$th column of H^{-1} into an $m \times n$ array. $\square$

For example, let h be the PSF generated by the MATLAB routine fspecial('gaussian', 5, 1) and $m = n = 15$. In figures 2(a) and (b), we show the signs of the real parts and the imaginary parts of some basis matrices. Note that only a 15×15 subregion of each matrix at 10:24 rows and 10:24 columns is shown for better visualization. The absolute value of eigenvalues are shown in figure 2(c), in which the stars corresponding to the basis matrices shown in figures 2(a) and (b). The red stars correspond to large $|\lambda_j|$ and the green stars correspond to small $|\lambda_j|$. It is easy to see that the basis matrices corresponding to small $|\lambda_j|$ tend to have more oscillation information while the basis matrices corresponding to large $|\lambda_j|$ have less oscillation information. We plot the absolute value of the eigenvalues of H^{-1} in figure 2(d) in which the star points are corresponding to figure 2(c). We show signs of the inverse matrix and signs of the inverse filter in figures 2(e) and (f) respectively. The oscillations of signs are obvious in the inverse filter.

In the following, we give some tests on the image deconvolution problems to further illustrate our observations. We consider three typical PSFs widely used in the image deconvolution problems: Gaussian kernel (Gaussian blur), motion kernel (motion blur) and disk kernel (out-of-focus blur). In figure 3, we display the PSFs and their inverse filters when applied on the standard test image 'Cameraman'. It is shown that the inverse filters can recover very high quality images. We can observe from figure 3 that all the inverse filters have oscillation patterns. This motivates us to use the texture norm as a prior for the inverse filters. We choose the Meyer's G space and the corresponding star norm defined for the continuous problems in Meyer (2001). It is proved in (Meyer (2001), lemma 14) that the oscillation functions have a small G norm.

Note that for the two-dimensional deconvolution problems the PSFs shown in figure 3 have some symmetric properties from the view point of matrix theory. For instance, the Gaussian PSF is rotationally symmetric, that is, $h_{\mathcal{R}(j,k)} = h_{j,k}$ for all 2D rotation transform $\mathcal{R}(j,k)$ and $j, k = -l, \ldots, l$. The out-of-focus PSF is symmetric, i.e. $h_{j,k} = h_{k,j}$. The motion PSF
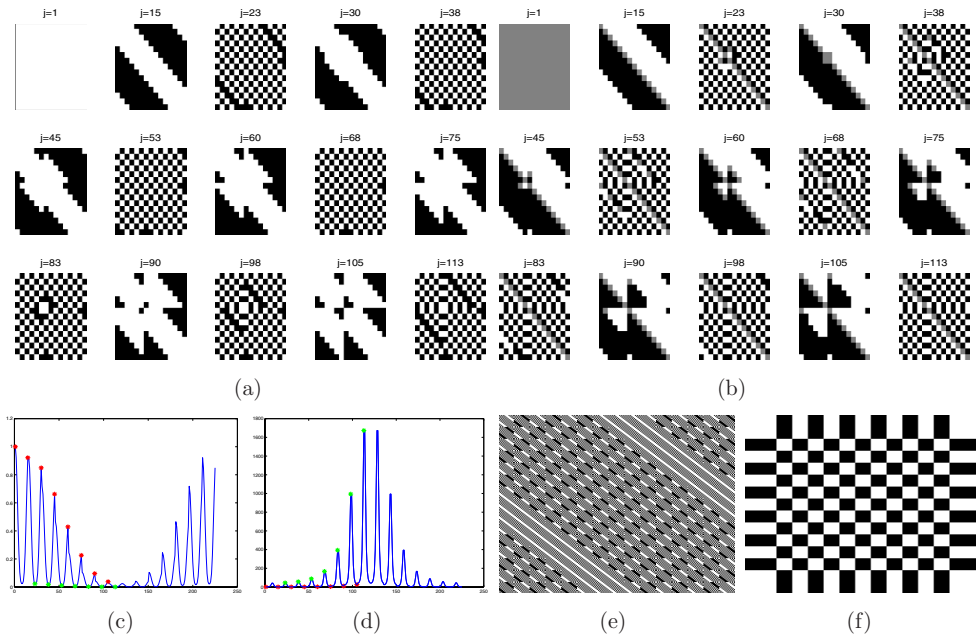
Figure 2. 2D example: $h =$ fspecial('gaussian', 5, 1), $m = n = 15$. (a) Signs of the real parts in subregions of some basis matrices (size: 15×15); (b) signs of the imaginary parts in subregions of some basis matrices (size: 15×15); (c) the absolute value of eigenvalues for H; (d) the absolute value of eigenvalues for the inverse matrix H^{-1}; (e) signs of the inverse matrix (size: 225×225); (f) signs of the inverse filter (size: 15×15). (In (a), (b), (e) and (f), white: positive elements, black: negative elements, gray: zero elements).

is centrosymmetric, i.e. $h_{j,k} = h_{-j,-k}$. Note that some usually used PSFs h are persymmetric, i.e. $h_{j,k} = h_{-k,-j}$. It is not difficult to show that the inverse filter u has similar symmetry properties as h. More precisely, if h is rotationally symmetric, symmetric, persymmetric or centrosymmetric, then so is its inverse filter u. These symmetric properties can be proved by straightforward computation and we omit the proof here.

2.3. Pseudo inverse filter

If the blurring matrix H is not invertible, we will find the pseudo inverse filter. In order to construct the pseudo inverse filter, instead of solving $Hf = g$, we compute the following least squares problem:

$$\min_{f} \|Hf - g\|_2^2.\tag{4}$$

The least square problem has a unique least-squares solution $f = H^+ g$ of smallest norm (Golub and Van Loan 2012), where the pseudo inverse matrix H^+ is given by

$$H^+ = \sum_{j=1,\lambda_j \neq 0}^{n} \frac{1}{\lambda_j} F_j^* F_j.$$
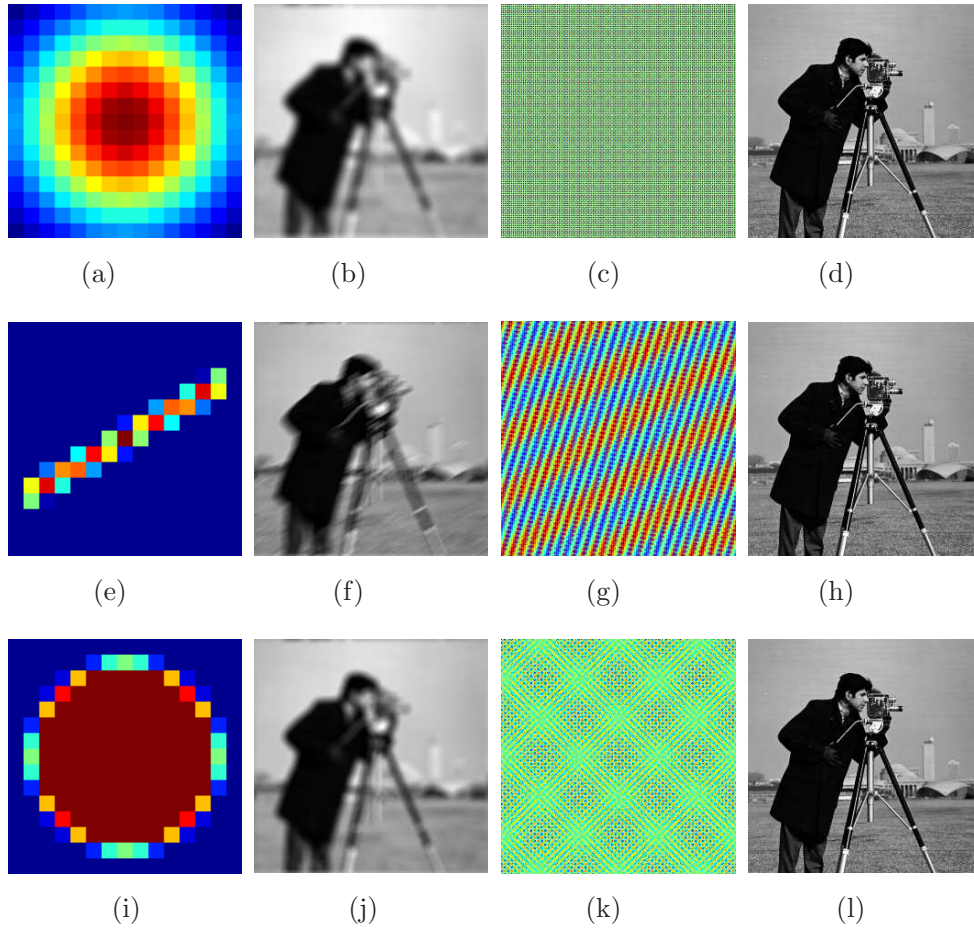
Figure 3. Examples of PSFs and their inverse filters. First column: From top to bottom are PSFs of Gaussian blur, motion blur and out-of-focus blur which are generated by the MATLAB routines fspecial('gaussian',15, 5), fspecial('motion',15, 30) and fspecial('disk', 6). Second column: the blurred images with PSFs in the first column. Third column: the inverse filters. Last column: the deblurred results using inverse filter by formula (2). (a) Guassian PSF. (b) PSNR = 19.95 dB. (c) inverse filter. (d) PSNR = 183.18 dB. (e) Motion PSF. (f) PSNR = 20.33 dB. (g) inverse filter. (h) PSNR = 231.85 dB. (i) Disk PSF. (j) PSNR = 20.35. (k) inverse filter. (l) PSNR = 240.80.

Similar as the construction of the inverse filter, we choose the same column of the pseudo inverse matrix H^+ to construct the pseudo inverse filter. Similar as the analysis and observation in section 2.2, we obtain that the pseudo inverse filter still has oscillation structure. We refer the interested reader to Louis (1999), Zhang (1997) and Pratt (2013) and references therein for the pseudo inverse filter.

Now let us consider the image degradation model (1) with noise. We aim to find the inverse filter u, such that

$$u * g = f. \tag{5}$$

Denote h^{-1} as the inverse filter constructed from H^{-1} if H is invertible and h_+^{-1} as the pseudo inverse filter constructed from H^+ if H is not invertible. Then we have

$$h^{-1} * g = f + h^{-1} * \eta$$

or

$$h_+^{-1} * g = f + h_+^{-1} * \eta.$$

Both filters will generally yield high frequency amplification of the additive noise, thereby corrupting the estimate of the original image. Moreover, the construction of h^{-1} and h_+^{-1} depends on the fact that h is known which is limited in real applications. In this paper, we propose to solve the inverse filter u by minimizing a new objective function without any known information about h. The objective function is convex such that the existence of inverse filter is guaranteed.

3. The proposed model

Firstly, let us introduce some notations. As in Chambolle (2004), the discrete gradient operator $\nabla : \mathbb{R}^{m \times n} \to (\mathbb{R}^{m \times n}, \mathbb{R}^{m \times n})$ is defined by

$$(\nabla v)_{j,k} = ((\nabla_1 v)_{j,k}, (\nabla_2 v)_{j,k})$$

with

$$(\nabla_1 v)_{j,k} = \begin{cases} v_{j+1,k} - v_{j,k}, & \text{if } j < m, \\ v_{1,k} - v_{m,k}, & \text{if } j = m \end{cases}$$

and

$$(\nabla_2 v)_{j,k} = \begin{cases} v_{j,k+1} - v_{j,k}, & \text{if } k < n, \\ v_{j,1} - v_{j,n}, & \text{if } k = n \end{cases}$$

for $j = 1, \ldots, m$ and $k = 1, \ldots, n$, where $v_{j,k}$ represents the value of pixel (j,k) in the image. The discrete divergence operator $\text{div} : (\mathbb{R}^{m \times n}, \mathbb{R}^{m \times n}) \to \mathbb{R}^{m \times n}$ is defined by

$$(\text{div} w)_{j,k} = (\nabla^T w)_{j,k} := (\nabla_1^T w^1)_{j,k} + (\nabla_2^T w^2)_{j,k}$$

with

$$(\nabla_1^T w^1)_{j,k} = \begin{cases} w_{m,k}^1 - w_{1,k}^1, & \text{if } j = 1, \\ w_{j-1,k}^1 - w_{j,k}^1, & \text{if } j > 1 \end{cases}$$

and

$$(\nabla_2^T w^2)_{j,k} = \begin{cases} w_{j,n}^2 - w_{j,1}^2, & \text{if } k = 1, \\ w_{j,k-1}^2 - w_{j,k}^2, & \text{if } k > 1 \end{cases}$$

for $j = 1, \ldots, m$ and $k = 1, \ldots, n$, where ∇^T is the adjoint of the operator ∇.

From Meyer (2001), we know that the discrete form of G-norm (star norm) $\|u\|_\star$ can be written as

$$\|u\|_\star = \inf\{\|w\|_\infty | u = \text{div} w, w = (w^1, w^2) \in (\mathbb{R}^{s \times s}, \mathbb{R}^{s \times s}),$$
$$|w_{j,k}| = \sqrt{(w_{j,k}^1)^2 + (w_{j,k}^2)^2}\}$$

where $\|w\|_\infty = \max_{j,k} |w_{j,k}| := \max_{j,k} \sqrt{(w_{j,k}^1)^2 + (w_{j,k}^2)^2}$. It has been proved that the oscillation functions have small G norms.

Let us reformulate our blind image restoration method as follows. Given the degraded image

$$g = h * f + n,$$

our aim is to find the inverse filter u such that

$$f = \begin{cases} \max\{u * g, 0\}, & (j,k) \in S, \\ f_B, & (j,k) \in \bar{S}. \end{cases}$$

where S is the support region, $\bar{S} = \Omega/S$ is the background region, and Ω is the image domain, f_B is the background intensity. In other words, the background region of the true image is known and f is nonnegative in the proposed method. Note that in the NAS-RIF method f_B is assumed to be constant. In this paper, the background of the image to recover is known but not necessary to be uniformly gray, black, or white. This occurs in certain types of image processing tasks with the known blurred region and real background. Note that the support region can be identified by the method proposed in Ong and Chambers (1999).

Based on the discussion in section 2.1, we consider the blind deconvolution of images using the following convex minimization model:

$$\min_u J(u) = \frac{\alpha}{2} J_1(u) + \beta J_2(u) + \gamma J_3(u) + \frac{1}{2} J_4(u), \tag{6}$$

where

$$\begin{aligned} J_1(u) &= \left(e_s^T u e_s - 1 \right)^2, \\ J_2(u) &= \|\nabla(u * g)\|_1, \\ J_3(u) &= \|u\|_\star, \\ J_4(u) &= \|u * g - P(u * g)\|_F^2. \end{aligned}$$

In the proposed model, $g \in \mathbb{R}^{m \times n}$ is the degraded image, $u \in \mathbb{R}^{s \times s}$ is the inverse filter to be determined, $e_s = (1, \ldots, 1)^T$ denotes a vector with length of s, $e_s^T u e_s$ is the sum of all elements of the inverse filter u, α, γ and β are nonnegative regularization parameters. $P(v)$ is the projection operator defined as

$$P(v) = \begin{cases} \max\{v, 0\}, & (j,k) \in S, \\ f_B, & (j,k) \in \bar{S}. \end{cases} \tag{7}$$

Let us give an interpretation of each term of the model. The first term $J_1(u)$ requires that the summation of inverse filter u equals one, which is reasonable for a filter. We know that the frequency response of the Dirac function $\delta = u * h$ at the origin is represented by $\mathcal{F}(u)(0,0) \cdot \mathcal{F}(h)(0,0) = 1$. Since the energy of an image is not absorbed and generated in the imaging system, the Fourier transformation of PSF at the origin is equal to one (Benvenuto *et al* 2009, Ding and Ren 2014). Thus, we have $\mathcal{F}(h)(0,0) = e_s^T h e_s = 1$. So it is clear that $\mathcal{F}(u)(0,0) = e_s^T u e_s = 1$.

The second term $J_2(u)$ is the total variation regularization term. It can preserve the edge information of the restored image $u * g$ (Rudin *et al* 1992, Vese 2001, Aubert and Kornprobst 2006). The third term $J_3(u)$ is motivated by the observation in section 2 that the inverse filter is oscillating.

The last term $J_4(u)$ is inspired by the NAS-RIF method where the support of blurred object is required (Kundur and Hatzinakos 1998). Using the projection operator P and the support S, we have

$$u * g - P(u * g) = \begin{cases} \min\{u * g, 0\}, & (i,j) \in S, \\ u * g - f_B, & (i,j) \in \bar{S}. \end{cases} \tag{8}$$

Minimizing the term $J_4(u)$ is equal to penalizing the negative pixels inside the region of support and penalizing the pixels outside the region of support that are not equal to the background intensity. In other words, $J_4(u)$ asks that the restored image satisfies the nonnegative constraint and background constraint.

If the proposed model is strictly convex, then it admits a unique minimizer. In the following, we show that the proposed model is strictly convex with respect to u.

Theorem 3.1. *The functional $J(u)$ in (6) is convex. If the Fourier transform of g satisfies $\mathcal{F}(g)(\xi, \eta) \neq 0$ for all (ξ, η), then $J(u)$ is strictly convex.*

Proof. We will show that each component of $J(u)$ is convex. For any $u_1, u_2 \in R^{s \times s}$ and $\lambda \in [0, 1]$, we need to prove

$$J_i(\lambda u_1 + (1 - \lambda)u_2) \leqslant \lambda J_i(u_1) + (1 - \lambda)J_i(u_2), i = 1, ..., 4. \tag{9}$$

For J_1 and J_2, the inequalities follow from the convexity of the quadratic function and the norm $\| \cdot \|_1$ respectively.

For J_3, assume $u_1 = \mathrm{div} w_{u_1}$ and $u_2 = \mathrm{div} w_{u_2}$ are two arbitrary decompositions of u_1 and u_2. Then $\lambda w_{u_1} + (1 - \lambda)w_{u_2}$ is an decomposition of $\lambda u_1 + (1 - \lambda)u_2$, that is,

$$\lambda u_1 + (1 - \lambda)u_2 = \mathrm{div}(\lambda w_{u_1} + (1 - \lambda)w_{u_2}).$$

By the convexity of L^∞ norm, we get

$$\|\lambda w_{u_1} + (1 - \lambda)w_{u_2}\|_\infty \leqslant \lambda \|w_{u_1}\|_\infty + (1 - \lambda)\|w_{u_2}\|_\infty.$$

Taking infimum on all the decompositions of u_1 and u_2, we get

$$\|\lambda u_1 + (1 - \lambda)u_2\|_\star \leqslant \lambda \|u_1\|_\star + (1 - \lambda)\|u_2\|_\star$$

which implies the convexity of J_3.

To prove the convexity of J_4, let us decompose the support region as non-overlapped regions S^+ and S^- which are defined as

$$S^+ := \{(j,k) \in S \,|\lambda u_1 * g + (1 - \lambda)u_2 * g \geqslant 0\},$$
$$S^- := \{(j,k) \in S \,|\lambda u_1 * g + (1 - \lambda)u_2 * g < 0\}.$$

Another decomposition of S as four non-overlapped regions $\Gamma^{++}, \Gamma^{+-}, \Gamma^{-+}$ and Γ^{--} is as follows:

$$\Gamma^{++} := \{(j,k) \in S \,|u_1 * g \geqslant 0, u_2 * g \geqslant 0\},$$
$$\Gamma^{+-} := \{(j,k) \in S \,|u_1 * g \geqslant 0, u_2 * g < 0\},$$
$$\Gamma^{-+} := \{(j,k) \in S \,|u_1 * g < 0, u_2 * g \geqslant 0\},$$
$$\Gamma^{--} := \{(j,k) \in S \,|u_1 * g < 0, u_2 * g < 0\}.$$

Using the decomposition, we can rewrite the left hand side of (9) for $i = 4$ as

$$J_4(\lambda u_1 + (1-\lambda)u_2)$$

$$= \|\lambda u_1 * g + (1-\lambda)u_2 * g - P(\lambda u_1 * g + (1-\lambda)u_2 * g)\|_F^2$$

$$= \begin{cases} 0, & (j,k) \in S^+ \\ \|\lambda u_1 * g + (1-\lambda)u_2 * g\|_F^2, & (j,k) \in S^- \\ \|\lambda u_1 * g + (1-\lambda)u_2 * g - f_B\|_F^2, & (j,k) \in \bar{S} \end{cases}$$

$$= \begin{cases} 0, & (j,k) \in S^+ \cap \Gamma^{++} \\ 0, & (j,k) \in S^+ \cap \Gamma^{+-} \\ 0, & (j,k) \in S^+ \cap \Gamma^{-+} \\ \|\lambda u_1 * g + (1-\lambda)u_2 * g\|_F^2, & (j,k) \in S^- \cap \Gamma^{+-} \\ \|\lambda u_1 * g + (1-\lambda)u_2 * g\|_F^2, & (j,k) \in S^- \cap \Gamma^{-+} \\ \|\lambda u_1 * g + (1-\lambda)u_2 * g\|_F^2, & (j,k) \in S^- \cap \Gamma^{--} \\ \|\lambda u_1 * g + (1-\lambda)u_2 * g - f_B\|_F^2, & (j,k) \in \bar{S} \end{cases}$$

and rewrite the right hand side of (9) for $i = 4$ as

$$\lambda J_4(u_1) + (1-\lambda)J_4(u_2)$$

$$= \lambda \|u_1 * g - P(u_1 * g)\|_F^2 + (1-\lambda)\|u_2 * g - P(u_2 * g)\|_F^2$$

$$= \begin{cases} 0, & (j,k) \in \Gamma^{++} \\ (1-\lambda)\|u_2 * g\|_F^2, & (j,k) \in \Gamma^{+-} \\ \lambda \|u_1 * g\|_F^2, & (j,k) \in \Gamma^{-+} \\ \lambda \|u_1 * g\|_F^2 + (1-\lambda)\|u_2 * g\|_F^2, & (j,k) \in \Gamma^{--} \\ \lambda \|u_1 * g - f_B\|_F^2 + (1-\lambda)\|u_2 * g - f_B\|_F^2, & (j,k) \in \bar{S} \end{cases}$$

$$= \begin{cases} 0, & (j,k) \in S^+ \cap \Gamma^{++} \\ (1-\lambda)\|u_2 * g\|_F^2, & (j,k) \in S^+ \cap \Gamma^{+-} \\ \lambda \|u_1 * g\|_F^2, & (j,k) \in S^+ \cap \Gamma^{-+} \\ (1-\lambda)\|u_2 * g\|_F^2, & (j,k) \in S^- \cap \Gamma^{+-} \\ \lambda \|u_1 * g\|_F^2, & (j,k) \in S^- \cap \Gamma^{-+} \\ \|\lambda u_1 * g + (1-\lambda)u_2 * g\|_F^2, & (j,k) \in S^- \cap \Gamma^{--} \\ \lambda \|u_1 * g - f_B\|_F^2 + (1-\lambda)\|u_2 * g - f_B\|_F^2. & (j,k) \in \bar{S} \end{cases}$$

By comparing the last expressions of the above two formulations in each region and using the convexity of the norm $\| \cdot \|_F^2$, we obtain that J_4 is convex. Note that another proof of convexity of J_4 can be found in Kundur and Hatzinakos (1998).

The equalities in the above derivation hold if and only if $(u - v) * g = 0$ and $e_s^T u e_s = e_s^T v e_s$. If $\mathcal{F}(g)(\xi, \eta) \neq 0$ for all (ξ, η), we have $u = v$, which implies the strictly convexity. □

4. The algorithm

In this section, we derive an efficient numerical algorithm based on the primal-dual method. It is known that many numerical methods can be employed to solve the proposed minimization

problem (6) due to its convexity. For instance, the alternating direction method with multipliers (ADMM) (Boyd *et al* 2011, Ouyang *et al* 2015), the split-Bregman algorithm (Goldstein and Osher 2009, Wu and Tai 2010), and the Chambolle-Pock algorithm (Chambolle and Pock 2011). In this paper, we use the Chambolle-Pock algorithm which solves a general saddle-point problem based on the primal-dual approach. The main reason is that, among the three algorithms, the Chambolle-Pock algorithm appears to be the fastest for non-smooth convex optimization problems arising in total variation regularization. It has been shown in Chambolle and Pock (2011) that the Chambolle-Pock algorithm has a convergence rate with one over the total number of iterations or more in some practical applications. In the following part, we briefly recall the Chambolle-Pock algorithm.

Let $M : X \to [0, +\infty]$ and $N^* : Y \to [0, +\infty]$ be proper, convex, lower semi-continuous, N^* be the convex conjugate of N. The Chambolle-Pock algorithm wants to solve the following general saddle-point problem:

$$\min_{x \in X} \max_{y \in Y} M(x) + \langle Kx, y \rangle - N^*(y), \tag{10}$$

where $K : X \to Y$ is a linear map with the induced norm

$$\|K\| = \max\{\|Kx\| : x \in X \text{ with } \|x\| \leqslant 1\}.$$

By choosing the parameter $\theta \in [0, 1]$ and initializing $(x^{(0)}, y^{(0)}) \in X \times Y$ and $\bar{x}^{(0)} = x^{(0)}$, Chambolle and Pock developed the following iteration scheme for solving the problem (10):

$$
\begin{aligned}
y^{(i+1)} &= (I + \tau_y \partial N^*)^{-1}(y^{(i)} + \tau_y K \bar{x}^{(i)}), \\
x^{(i+1)} &= (I + \tau_x \partial M)^{-1}(x^{(i)} - \tau_x K^* y^{(i+1)}), \\
\bar{x}^{(i+1)} &= x^{(i+1)} + \theta(x^{(i+1)} - x^{(i)}),
\end{aligned}
$$

where $\tau_x > 0$ and $\tau_y > 0$ are the given steps. We refer to Chambolle and Pock (2011) for more details.

Let us introduce two extra variables $v \in \mathbb{R}^{m \times n}$ and $w = (w^1, w^2) \in (\mathbb{R}^{s \times s}, \mathbb{R}^{s \times s})$, and reformulate the problem (6) as the following constrained optimization problem:

$$
\begin{aligned}
&\min_{u,v,w} \left\{ \frac{\alpha}{2}(e_s^T u e_s - 1)^2 + \beta \|\nabla v\|_1 + \gamma \|w\|_\infty + \frac{1}{2} \|v - P(v)\|_F^2 \right\} \\
&\text{subject to} \quad v = u * g, u = \text{div} w.
\end{aligned} \tag{11}
$$

Then we can employ the Chambolle-Pock algorithm for solving the proposed inverse filtering model (6) by considering the following primal-dual optimization problem:

$$
\max_{p,q,r} \min_{u,v,w} \left\{ \begin{array}{c} \frac{\alpha}{2}(e_s^T u e_s - 1)^2 + \beta \langle \nabla v, p \rangle + \gamma \|w\|_\infty + \frac{1}{2} \|v - P(v)\|_F^2 \\ \langle v - u * g, q \rangle + \langle u - \text{div} w, r \rangle - I_Q(p) \end{array} \right\}, \tag{12}
$$

where p, q and r are the dual variables. The convex set Q is given by

$$Q = \{p = (p^1, p^2) \in (\mathbb{R}^{m \times n}, \mathbb{R}^{m \times n}) \mid \|p\|_\infty \leqslant 1\}.$$

The function I_Q denotes the indicator function of the set Q, which is defined as

$$
I_Q(p) = \begin{cases} 0, & \text{if } p \in Q, \\ +\infty, & \text{otherwise.} \end{cases}
$$

Then the Chambolle-Pock algorithm is defined through the iteration scheme as follows. As for the dual variables p, q and r, we have

$$p^{(i+1)} = \arg\max_{p} \beta\langle\nabla\bar{v}^{(i)}, p\rangle - \frac{1}{2\sigma_p}\|p - p^{(i)}\|_F^2 - I_Q(p), \tag{13}$$

$$q^{(i+1)} = \arg\max_{q} \langle\bar{v}^{(i)} - \bar{u}^{(i)} * g, q\rangle - \frac{1}{2\sigma_q}\|q - q^{(i)}\|_F^2, \tag{14}$$

$$r^{(i+1)} = \arg\max_{r} \langle\bar{u}^{(i)} - \mathrm{div}\bar{w}^{(i)}, r\rangle - \frac{1}{2\sigma_r}\|r - r^{(i)}\|_F^2. \tag{15}$$

As for the primal variables u, v and w, we have

$$u^{(i+1)} = \arg\min_{u} \frac{\alpha}{2}(e_s^T u e_t - 1)^2 - \langle u * g, q^{(i+1)}\rangle + \langle u, r^{(i+1)}\rangle + \frac{1}{2\tau_u}\|u - u^{(i)}\|_F^2, \tag{16}$$

$$v^{(i+1)} = \arg\min_{v} \beta\langle v, \nabla^T p^{(i+1)}\rangle + \langle v, q^{(i+1)}\rangle + \frac{1}{2}\|v - P(v)\|_F^2 + \frac{1}{2\tau_v}\|v - v^{(i)}\|_F^2, \tag{17}$$

$$w^{(i+1)} = \arg\min_{w} \gamma\|w\|_\infty + \langle-\mathrm{div}w, r^{(i+1)}\rangle + \frac{1}{2\tau_w}\|w - w^{(i)}\|_F^2. \tag{18}$$

As for the intermediate variables $\bar{u}$ and $\bar{v}$, we have

$$\bar{u}^{(i+1)} = 2u^{(i+1)} - u^{(i)}, \tag{19}$$

$$\bar{v}^{(i+1)} = 2v^{(i+1)} - v^{(i)}, \tag{20}$$

$$\bar{w}^{(i+1)} = 2w^{(i+1)} - w^{(i)}. \tag{21}$$

It is easy to derive the update formulas of dual variables p, q, r. For p, we have

$$p_{j,k}^{(i+1)} = (p^{(i)} + \beta\sigma_p\nabla\bar{v}^{(i)})_{j,k} / \max(|(p^{(i)} + \beta\sigma_p\nabla\bar{v}^{(i)})_{j,k}|, 1) \tag{22}$$

for $j = 1, \ldots, m$ and $k = 1, \ldots, n$, where $|p_{j,k}| = \sqrt{(p_{j,k}^1)^2 + (p_{j,k}^2)^2}$. As for q and r, we have

$$q^{(i+1)} = q^{(i)} + \sigma_q(\bar{v}^{(i)} - \bar{u}^{(i)} * g), \tag{23}$$

$$r^{(i+1)} = r^{(i)} + \sigma_r(\bar{u}^{(i)} - \mathrm{div}\bar{w}^{(i)}). \tag{24}$$

By using the equality $\langle u * g, q^{(i+1)}\rangle = \langle u, g' * q^{(i+1)}\rangle$ where g' is obtained from g through a horizontal and a vertical flip, we obtain that the update formula of u in subproblem (16) is given as

$$\mathrm{Vec}(u^{(i+1)}) = (I + \tau\alpha e_{s^2} e_{s^2}^T)^{-1} \cdot \mathrm{Vec}(u^{(i)} + \tau_u(\alpha e_s e_s^T + g' * q^{(i+1)} - r^{(i+1)})),$$

where $\mathrm{Vec}(u)$ denotes a vector obtained by stacking all the elements in the matrix u along columns. This is a symmetric positive definite problem. Usually, the solution can be computed by the conjugate gradient method (Ding *et al* 2015). In this paper, we use a simple direct method. Using the Sherman-Morrison-Woodbury formula (Sherman and Morrison 1950), we have

$$(I + \tau\alpha e_{s^2} e_{s^2}^T)^{-1} = I - \frac{\tau\alpha}{\tau_u\alpha s^2 + 1} e_{s^2} e_{s^2}^T.$$

So we get

$$\text{Vec}(u^{(i+1)}) = \left(I - \frac{\tau\alpha}{\tau_u\alpha s^2 + 1}e_{s^2}e_{s^2}^T\right)\cdot \text{Vec}(u^{(i)} + \tau_u(\alpha e_s e_s^T + g' * q^{(i+1)} - r^{(i+1)})). \tag{25}$$

To get the update formula of v in the subproblem (17), let us introduce two indicator functions:

$$I_s(v_{j,k}) = \begin{cases} 1, & (j,k) \in S, \\ 0, & (j,k) \in \bar{S} \end{cases}$$

and

$$I_n(v_{j,k}) = \begin{cases} 1, & v_{j,k} < 0, \\ 0, & v_{j,k} \geqslant 0. \end{cases}$$

With the notations, we have

$$v - P(v) = (I - I_s)(v - f_B) + I_s I_n(v).$$

Then, the update equation of v is given as

$$v_{j,k}^{(i+1)} = \left(v^{(i)} + \tau_v(I - I_s)f_B - \tau_v(\beta\nabla^T p^{(i+1)} + q^{(i+1)})\right)_{j,k} / \left(\tau_v(I - I_s + I_s I_n)_{j,k} + 1\right) \tag{26}$$

for $j = 1,\ldots,m$ and $k = 1,\ldots,n$. For the w subproblem (18), we have

$$w^{(i+1)} = \arg\min_w \|w\|_\infty + \frac{1}{\tau_w}\|w - (w^{(i)} + \tau_w\nabla r^{(i+1)})\|_F^2. \tag{27}$$

It follows from Combettes and Wajs (2005) that

$$w^{(i+1)} = w^{(i)} + \tau_w\nabla r^{(i+1)} - P_\Omega(w^{(i)} + \tau_w\nabla r^{(i+1)}), \tag{28}$$

where P_Ω is the projection operator onto $\Omega = \{w \in (\mathbb{R}^{s\times s}, \mathbb{R}^{s\times s}), \|w\|_1 \leqslant \tau_w\}$.

Finally, the Chambolle-Pock algorithm used to solve the optimization problem (6) is summarized as in algorithm 1.

Algorithm 1.

- Initialization: Choose $\tau_u, \tau_v, \tau_w, \tau_p, \tau_q, \tau_r > 0$, $u^0 = \delta$, $v^0 = g$, $w^0 = \mathbf{0}$, $p^0 = \mathbf{0}$, $q^0 = \mathbf{0}$, $r^0 = \mathbf{0}$.
- For $k = 0, 1, 2, \ldots$, repeat until stoping criterion is reached
  Update p, q, r by (22), (23) and (24) respectively;
  Update u, v, w by (25), (26) and (28) respectively;
  Update $\bar{u}, \bar{v}, \bar{w}$ by (19), (20) and (21) respectively.
- Output: $u^{k+1}*g$.

To enhance the numerical stability, we add the symmetry constraints as discussed in section 2 immediately after u is updated in algorithm 1. The constraints are realized by $u_{\text{sym}} = (u + u^T)/2$ for the symmetric case, $u_{\text{persym}} = (u + Ju^T J)/2$ for the persymmetric case and $u_{\text{centrosym}} = (u + JuJ)/2$ for the centrosymmetric case, where J is the reverse identity matrix, i.e. J has ones on the cross diagonal and zeros elsewhere.

In the following, we discuss the convergence of the proposed algorithm 1. Define

$$K = \begin{pmatrix} 0 & \beta\nabla & 0 \\ -A & I & 0 \\ I & 0 & -\text{div} \end{pmatrix}, \quad x = \begin{pmatrix} u \\ v \\ w \end{pmatrix}, \quad \bar{x} = \begin{pmatrix} \bar{u} \\ \bar{v} \\ \bar{w} \end{pmatrix}, \quad y = \begin{pmatrix} p \\ q \\ r \end{pmatrix},$$

where A denotes the operator satisfying $Au := u * g$. For ease of presentation, we take x, $\bar{x}$, y and related variables as vectors by the stacking scheme. Since $\|Au\|_2 = \|u * g\|_2 \leqslant \|g\|_1 \|u\|_2$ (lemma 1.4 in Bahouri *et al* (2011)), it is not difficult to show that $\|A\|_2$ is bounded for given g. Then the primal-dual problem (12) is equivalent to

$$\max_y \min_x M(x) + \langle Kx, y \rangle - N^*(y) \tag{29}$$

where

$$M(x) = \frac{\alpha}{2}(e_s^T u e_t - 1)^2 + \gamma \|w\|_\infty + \frac{1}{2}\|v - P(v)\|_2^2,$$
$$N^*(y) = I_Q(p).$$

By a similar argument as in (Ma *et al* 2013, proposition 2), we know that the saddle-point set of (29) is nonempty. Then we have the convergence of algorithm 1 as below.

Proposition 4.1. *Denote $\|K\|_2$ the operator 2-norm of K. Let $(x^k, \bar{x}^k, y^k)$ be the sequence defined by algorithm 1. If we choose $\tau_u, \tau_v, \tau_w, \tau_p, \tau_q, \tau_r$ such that*

$$\max\{\tau_u, \tau_v, \tau_w\} \cdot \max\{\tau_p, \tau_q, \tau_r\} < 1/\|K\|_2^2,$$

then the sequence (x^k, y^k) converges to the saddle point $(\hat{x}, \hat{y})$ of (29).

The proposition is a special case of theorem 1 in Chambolle and Pock (2011). By the equivalence of the problem (29) to the problem (11) (Ekeland and Temam 1976), we get that $\hat{u}$ is a solution of (6). In addition, we have the following estimation for $\|K\|_2$. To get the bound of operator K, we estimate

$$\begin{aligned}
\|Kx\|_2 &= \left\| \begin{pmatrix} \beta\nabla u \\ -Au + v \\ u - \text{div}w \end{pmatrix} \right\|_2 \\
&\leqslant \left\| \begin{pmatrix} \beta\nabla u \\ -Au \\ u \end{pmatrix} \right\|_2 + \left\| \begin{pmatrix} v \\ -\text{div}w \end{pmatrix} \right\|_2 \\
&= \sqrt{\|\beta\nabla u\|_2^2 + \|Au\|_2^2 + \|u\|_2^2} + \sqrt{\|v\|_2^2 + \|\text{div}w\|_2^2} \\
&\leqslant \sqrt{\|\beta\nabla\|_2^2 + \|A\|_2^2 + 1} \cdot \|u\|_2 + \sqrt{1 + \|\text{div}\|_2^2} \cdot \sqrt{\|v\|_2^2 + \|w\|_2^2} \\
&\leqslant \sqrt{\beta^2\|\nabla\|_2^2 + \|A\|_2^2 + \|\text{div}\|_2^2 + 2} \cdot \|x\|_2.
\end{aligned}$$

Hence we get the estimation

$$\|K\|_2 \leqslant \sqrt{\beta^2\|\nabla\|_2^2 + \|A\|_2^2 + \|\text{div}\|_2^2 + 2}.$$

Moreover, since $\|\nabla\|_2^2 \leqslant 8$ (Chambolle 2004), we have $\|\text{div}\|_2^2 = \|\nabla^T\|_2^2 \leqslant 8$. Thus
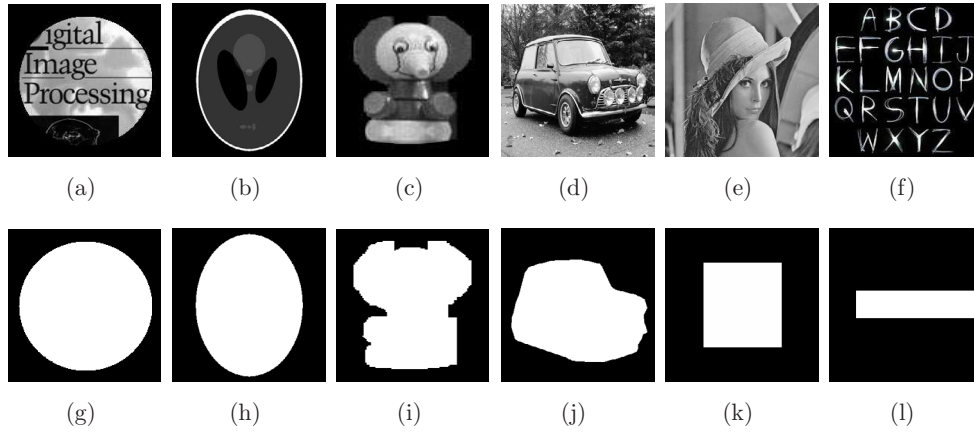
Figure 4. Test data set. (a)–(c) test images with uniform black background; (d)–(f) test images with nonuniform background; (g)–(l) the support regions of (a)–(f) respectively. Figure 4(a) reproduced with permission from Gonzalez R C, Woods R E., Digital Image Processing. Addison-Wesley, 2010. Figure 4(b) this "SheppLogan Phantom.svg" image has been obtained by the author(s) from the Wikimedia website where it was made available by Bitic under a CC BY-SA 4.0 licence. It is included within this article on that basis. It is attributed to Larry Shepp and Benjamin F Logan. Figure 4(c) reproduced with permission from Kundur, D. & Hatzinakos, D. (1998). IEEE Transactions on Signal Processing 46(2): 375–390. © Copyright 1998 IEEE. Figure 4(d) reproduced with permission from Best Car Magazine. Figure 4(e) © Playboy Enterprises, Inc. Figure 4(f) reproduced with permission from http://newgrafitimakmu.blogspot.com/2010/01/graffiti-alphabet-letter-fonts-z-light.html.

$$\|K\|_2 \leqslant \sqrt{\|A\|_2^2 + 8\beta^2 + 10},$$

where β is a given nonnegative regularization parameter and $\|A\|_2$ is bounded.

5. Experiments and comparisons

In this section, we illustrate the performance of our proposed method for blind deconvolution of images by comparing it with the following closely related methods:

DTV: Double TV (DTV) method was given in Chan and Wong (1998) where the TV regularization is used on both the image and the kernel. The motivation for regularizing with the TV norm is that it is extremely effective for recovering edges of images as well as some blurring kernels such as motion blur and out-of-focus blur.

IBD: Iterative blind deconvolution (IBD) proposed in Ayers and Dainty (1988) is an iterative Wiener type filtering method. In the iterative process, IBD recovers the original image and estimates the PSF alternately. In addition, the resulted algorithm switches between the space and Fourier domains, enforcing known constraints in each.

NAS-RIF: Nonnegativity and support constraints recursive inverse filtering (NAS-RIF) method was presented in Kundur and Hatzinakos (1998) for blind image restoration. NAS-RIF consists of a variable finite impulse response filter with the blurred image as input. The output of the adaptive filter represents an estimate of the original image. This estimate is applied to a non-linear filter to project the estimated image into the space representing the known characteristics of the true image such as nonnegativity, bounds on the pixel amplitude

Table 1. SSIM and PSNR values by different methods for the test images with blur and without noise.

Blur	Image	DTV PSNR/ SSIM	IBD PSNR/ SSIM	NAS-RIF PSNR/SSIM	TV-RIF PSNR/SSIM	Ours PSNR/ SSIM
Gaussian	Cover	18.41/0.7848	17.10/0.7654	19.45/0.8655	18.21/0.8360	**21.83/ 0.8914**
	Phantom	23.52/0.9644	20.85/0.9435	24.96/0.9682	24.69/0.9676	**26.15/ 0.9688**
	Toy	24.83/0.8763	21.58/0.8378	26.87/0.8845	26.91/0.8847	**27.13/ 0.9176**
	Car	19.38/0.8544	18.07/0.8437	20.15/0.9094	21.49/0.9194	**23.01/ 0.9273**
	Lena	23.84/0.8958	21.47/0.8833	25.01/0.9283	25.94/0.9165	**26.00/ 0.9366**
	Letters	16.16/0.9415	15.70/0.9379	19.43/0.9496	20.05/0.9611	**21.19/ 0.9652**
Motion	Cover	18.99/0.8142	18.14/0.5688	17.54/0.7899	18.25/0.8401	**22.55/ 0.8684**
	Phantom	25.04/0.9451	23.05/0.9234	21.16/0.9432	23.05/0.9426	**25.63/ 0.9495**
	Toy	25.02/0.7145	22.74/0.7091	26.11/0.8849	25.93/0.8822	**27.79/ 0.9041**
	Car	19.53/0.9021	18.51/0.8576	19.35/0.9038	20.13/0.9214	**23.83/ 0.9243**
	Lena	25.04/0.9357	23.05/0.9268	26.22/0.9491	27.67/0.9512	**29.31/ 0.9674**
	Letters	19.54/0.9407	16.45 /0.9097	19.59/0.9430	19.72/0.9527	**21.77/ 0.9538**
Defocus	Cover	18.38/0.7610	18.46/0.5422	18.07/0.7849	18.22/0.8315	**22.50/ 0.8716**
	Phantom	23.11/0.9307	24.00/0.9473	22.26/0.9434	24.21/0.9313	**26.77/ 0.9595**
	Toy	23.62/0.6121	23.23/0.5886	25.81/0.8810	27.42/0.8752	**27.52/ 0.9032**
	Car	19.13/0.8199	18.64/0.8183	19.24/0.8932	20.05/0.9151	**24.18/ 0.9231**
	Lena	23.30/0.9013	22.34/0.9040	23.62/0.9067	26.87/0.9448	**27.30/ 0.9483**
	Letters	20.96/0.9564	17.04/0.9458	20.14/0.9428	20.87/0.9547	**22.50/ 0.9601**
	Average	21.61/0.8639	20.02/0.8252	21.94/0.9040	22.76/0.9127	**24.83/ 0.9300**

and finite support in many real gray scale images. The output of this non-linear filter is the estimated image we want to recover.

TV-RIF: TV-based regularized inverse filtering method (TV-RIF) was investigated in Wang and Ng (2016) for blind deconvolution of images. The main idea of TV-RIF is to make use of nonnegativity and support constraints, and to incorporate regularization terms to establish a convex programming model which aims to determine an inverse filter for image deconvolution.

In this paper, all computations were carried out in Matlab R2014a. The results were obtained by running the Matlab codes on an Intel(R) Core(TM) i7-4790 CPU (3.60 GHz, 3.60 GHz) computer with RAM of 8 GB. To evaluate the restoration quality, we use the peak signal-to-noise ratio (PSNR) and structural similarity (SSIM) index. PSNR is defined by

$$\text{PSNR} = 10\log_{10}\left(\frac{mn \cdot \text{Max}_f^2}{\|\tilde{f} - f\|_2^2}\right), \tag{30}$$

where f and $\tilde{f}$ are the $m \times n$ ideal image and the restored image respectively, and Max_f is the maximum possible pixel value of the image f. For example, when the pixels are represented by 8 bits per sample, the value of Max_f is 255. The definition of SSIM can be found in Wang *et al* (2004). The SSIM index assesses the conservation of the structural information of the restored image. Note that the perfect restoration would have the SSIM value equal to 1. The larger the value of SSIM is, the better the quality of restoration will be.

In the experiments, we apply three kinds of commonly used PSFs generated by matlab routines as follows:

- fspecial('gaussian',15, 2), Gaussian blur with standard deviation 2, size 15×15;
- fspecial('motion',7, 45), motion blur with 7 pixels along 45 degree, size 7×7;
- fspecial('disk', 2), out-of-focus (defocus) blur with size 5×5.

Table 2. SSIM and PSNR values by different methods for the test images with blur and noise of BSNR = 30 dB.

Blur	Image	DTV PSNR/ SSIM	IBD PSNR/ SSIM	NAS-RIF PSNR/SSIM	TV-RIF PSNR/SSIM	Ours PSNR/ SSIM
Gaussian	Cover	18.50/0.7900	17.04/0.7627	17.20/0.7612	17.61/0.7659	**19.30/ 0.8119**
	Phantom	23.26/0.9316	20.77/0.9119	22.81/0.9144	22.97/0.9283	**24.22/ 0.9348**
	Toy	24.77/0.8717	21.54/0.8365	22.28/0.8567	24.65/0.8673	**25.20/ 0.8741**
	Car	19.30/0.8514	18.05/0.8419	19.07/0.8609	19.79/0.8590	**20.81/ 0.8618**
	Lena	23.73/0.8945	21.47/0.8835	23.64/0.9013	24.37/0.9121	**24.74/ 0.9125**
	Letters	16.18/0.9421	15.65/0.9376	19.28/0.9464	19.40/0.9430	**19.90/ 0.9510**
Motion	Cover	15.80/0.7634	12.40/0.5365	16.74/0.7710	18.07/0.7896	**21.31/ 0.8451**
	Phantom	17.99/0.9154	21.99/0.8715	21.75/0.9219	23.54/0.9287	**24.94/ 0.9291**
	Toy	19.32/0.7620	19.28/0.7382	25.11/0.8812	26.34/0.8884	**26.81/ 0.8943**
	Car	19.03/0.8624	17.86/0.8077	18.50/0.8730	20.19/0.8808	**22.97/0.8831**
	Lena	23.72/0.9117	25.43/0.9331	24.54/0.9435	26.98/0.9490	**27.78/ 0.9498**
	Letters	19.73/0.9393	16.59/0.9359	17.53/0.9356	19.58/0.9369	**21.35/ 0.9485**
Defocus	Cover	16.92/0.7754	18.21/0.7735	17.20/0.7804	18.08/0.7784	**21.41/ 0.8499**
	Phantom	19.43/0.9287	18.11/0.8650	22.67/0.9348	24.71/0.9352	**25.94/ 0.9393**
	Toy	21.33/0.8197	17.43/0.6632	24.88/0.8585	26.64/0.8791	**26.90/ 0.8948**
	Car	18.97/0.8608	18.92/0.8292	17.54/0.8684	20.34/0.8795	**23.04/ 0.8834**
	Lena	21.08/0.8769	25.06/0.9201	24.86/0.9246	25.66/0.9279	**26.34/ 0.9348**
	Letters	14.13/0.9365	13.49/0.9125	18.28/0.9348	20.99/0.9388	**22.24/ 0.9552**
	Average	19.62/0.8685	18.85/0.8311	20.77/0.8816	22.22/0.8887	**23.62/ 0.9030**

We consider both the noise-free case and the noisy case with noise level of BSNR = 30 dB. The definition of blurred signal-to-noise ratio (BSNR) is given by

$$\mathrm{BSNR} = 10\log_{10}\left(\frac{\|g\|_2^2}{\|\eta\|_2^2}\right),$$

where g and η are the observed image and the Gaussian white noise respectively. In the competing methods, the initial guess for the PSF h or the inverse filter (PSF) u is chosen to be the delta function δ because in the case of no blurring δ would be the expected inverse filter. The sizes of the PSF or the inverse PSF for the three blurs are $7 \times 7, 11 \times 11$ and 17×17 pixels, respectively. The stopping criterion of all competing methods is that the maximum number of allowed outer iterations has been carried out or the relative differences between consecutive iterates of the inverse filter (for NAS-RIF, TV-RIF and our method) satisfy

$$\frac{\|u^{(k+1)} - u^{(k)}\|_2}{\|u^{(k+1)}\|_2} < \epsilon_1$$

or the relative differences between consecutive iterates of the estimated PSF (for DTV and IBD) satisfy

$$\frac{\|h^{(k+1)} - h^{(k)}\|_2}{\|h^{(k+1)}\|_2} < \epsilon_2.$$

In all tests, we set $\epsilon_1 = \epsilon_2 = 10^{-5}$ for all competing methods. The maximum number of outer iterations is 200 for IBD, NAS-RIF and RIF-TV while 1000 for DTV and our proposed method. In the NAS-RIF and RIF-TV methods, the subproblems need the conjugate gradient algorithm for the solution. The maximum number of allowed iterations for the conjugate gradient algorithm in the two methods is set to be 10. For the DTV method, the authors used
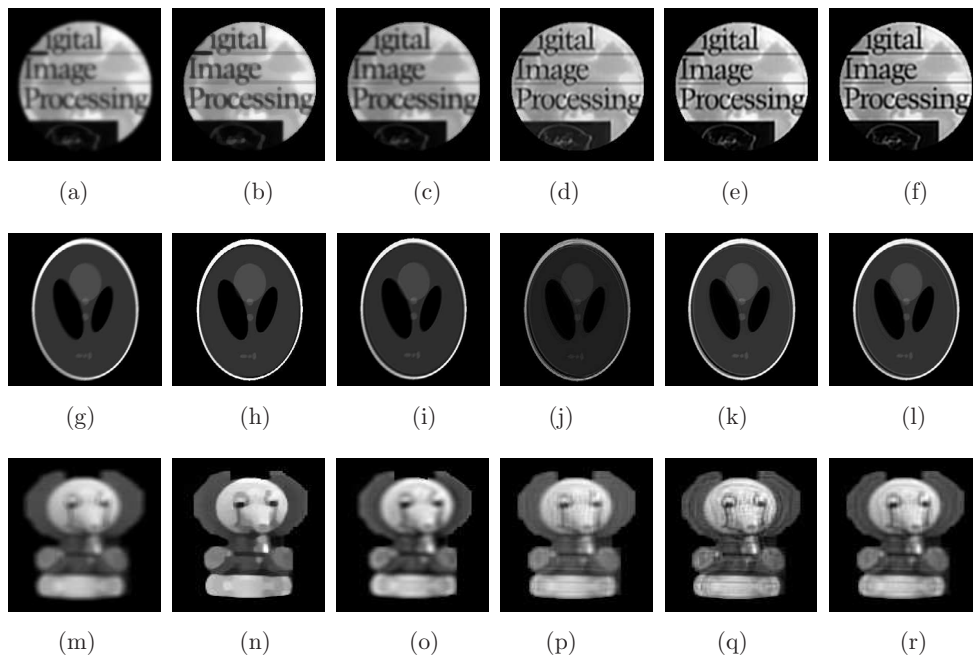
Figure 5. Comparison of results by different methods applied on blurred images with black background without noise. First column: the blurred images; Second to sixth columns: the restoration results by DTV, IBD, NAS-RIF, TV-RIF and ours respectively. (a) Gaussian. (b) DTV. (c) IBD. (d) NAS-RIF. (e) TV-RIF. (f) Ours. (g) Motion. (h) DTV. (i) IBD. (j) NAS-RIF. (k) TV-RIF. (l) Ours. (m) Defocus. (n) DTV. (o) IBD. (p) NAS-RIF. (q) TV-RIF. (r) Ours. Figures 5(a)–(f) reproduced with permission from Gonzalez R C, Woods R E., Digital Image Processing. Addison-Wesley, 2010. Figures 5(g)–(l) this "SheppLogan Phantom.svg" image has been obtained by the author(s) from the Wikimedia website where it was made available by Bitic under a CC BY-SA 4.0 licence. It is included within this article on that basis. It is attributed to Larry Shepp and Benjamin F Logan. Figure 5(m)-(r) reproduced with permission from Kundur, D. & Hatzinakos, D. (1998). IEEE Transactions on Signal Processing 46(2): 375–390. © Copyright 1998 IEEE.

the alternating minimization scheme to solve the double TV-based model. In this paper, we solve the double TV-based model with the ADMM method which is more efficient than the alternating minimization algorithm in the original paper; see Li *et al* (2012) for more details. As is well known, the quality of the restored image is highly dependent on the regularization parameters. In order to have fair comparisons in all tests for the competing methods, we determine the best values of the regularization parameters such that the PSNR value of the restored image with respect to the original image is the best. Positivity constraints are used for both images and PSFs in all tests. Additional constraints of image mean preservation and PSF symmetry are used to improve the restoration results.

In the conventional NAS-RIF algorithm, the background of the degraded images is assumed to be uniformly gray, black or white. In addition, the object is assumed to be contained within a rectangular region of support. However, for nonrectangular objects the real background pixels within the region of support will be wrongly classified as object pixels. In this paper, we assume that the support region is known. But the background of the degraded images is not necessary to be uniformly gray, black, or white. In figure 4, we show six test images in the first row and their support masks in the second row. The first three test images ('Cover,
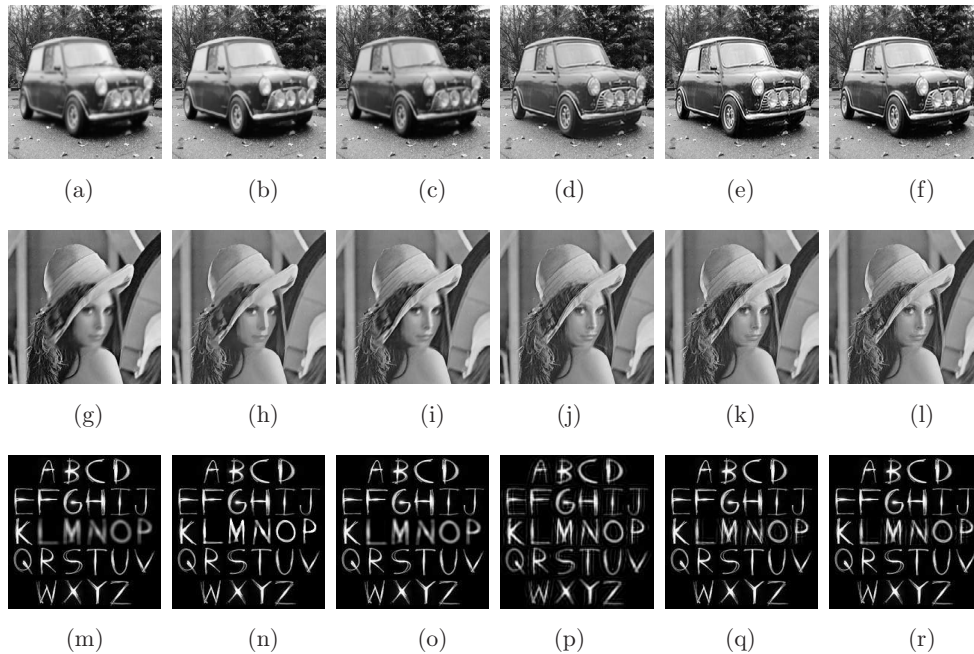
Figure 6. Comparison of results by different methods applied on blurred images with nonuniform background without noise. First column: the blurred images; Second to sixth columns: the restoration results by DTV, IBD, NAS-RIF, TV-RIF and ours respectively. (a) Gaussian. (b) DTV. (c) IBD. (d) NAS-RIF. (e) TV-RIF. (f) Ours. (g) Motion. (h) DTV. (i) IBD. (j) NAS-RIF. (k) TV-RIF. (l) Ours. (m) Defocus. (n) DTV. (o) IBD. (p) NAS-RIF. (q) TV-RIF. (r) Ours. Figures 6(a)–(f) reproduced with permission from Best Car Magazine. Figures 6(g)–(l) © Playboy Enterprises, Inc. Figures 6(m)–(r) reproduced with permission from http://newgrafitimakmu.blogspot.com/2010/01/graffiti-alphabet-letter-fonts-z-light.html.

Phantom, Toy') in figure 4 have uniform background (black background), while the last three test images ('Car, Lena, Letters') in figure 4 have nonuniform background.

For quantitative comparison, we report the PSNR and SSIM values obtained by each method on all test images degraded by different blurs in tables 1 and 2. Clearly, table 1 includes the comparison results for the noise-free case while table 2 for the noisy case with noise level of BSNR = 30 dB. The highest PSNR and SSIM values for each case are highlighted in bold. From the tables, it is easy to see that the proposed method achieves higher PSNR and SSIM values than DTV, IBD, NAS-RIF, TV-RIF on all test images. For example, the PSNR average gain of our method over DTV, IBD, NAS-RIF, TV-RIF is as much as 2.93 dB, 5.42 dB, 2.10 dB and 1.61 dB respectively on 'letters' image for the noise-free case. On average, our method gains 4.48 dB, 5.92 dB, 2.80 dB and 1.17 dB more than DTV, IBD, NAS-RIF, TV-RIF respectively on the same image in the noisy case. The proposed method performs better, with SSIM average values 0.9300 versus 0.8639, 0.8252, 0.9040 and 0.9127 in the DTV, IBD, NAS-RIF and TV-RIF algorithms on all test images for the noise-free case while with SSIM average values 0.9030 versus 0.8685, 0.8311, 0.8816 and 0.8887 for the noisy case. From tables 1 and 2, our proposed method outperforms the other four methods for blind deconvolution of images under both the noise-free case and the noisy case.

For visual comparison of the recovered images, some of the restoration results are selected to display in figures 5–8. The first column are blurred images. The second to sixth columns are
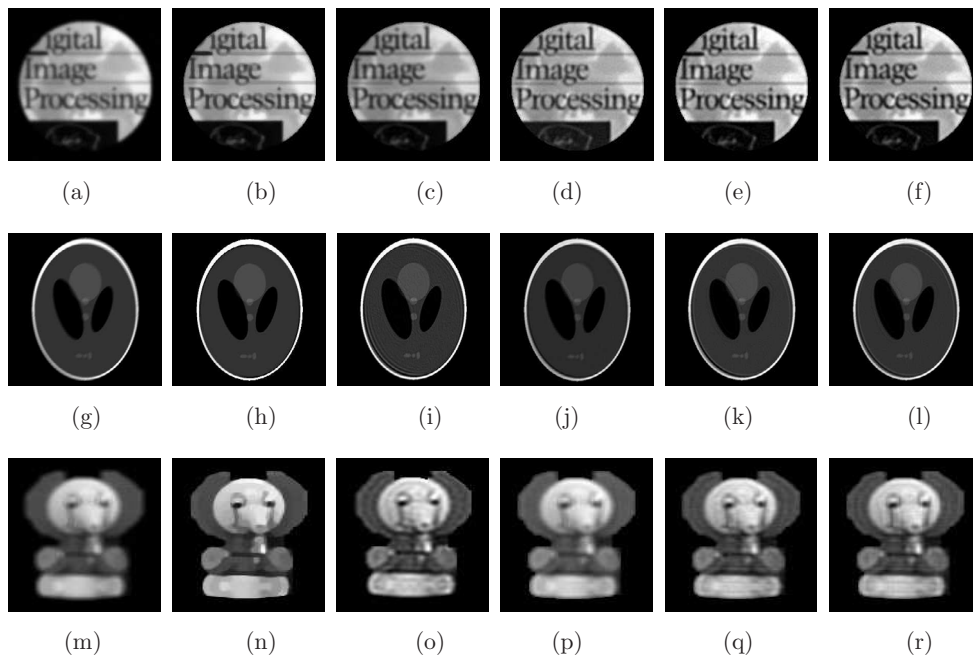
Figure 7. Comparison of results by different methods applied on blurred images with black background and noise of BSNR = 30 dB. First column: the blurred images; Second to sixth columns: the restoration results by DTV, IBD, NAS-RIF, TV-RIF and ours respectively. (a) Gaussian. (b) DTV. (c) IBD. (d) NAS-RIF. (e) TV-RIF. (f) Ours. (g) Motion. (h) DTV. (i) IBD. (j) NAS-RIF. (k) TV-RIF. (l) Ours. (m) Defocus. (n) DTV. (o) IBD. (p) NAS-RIF. (q) TV-RIF. (r) Ours. Figures 7(a)–(f) reproduced with permission from Gonzalez R C, Woods R E., Digital Image Processing. Addison-Wesley, 2010. Figures 7(g)–(l) this "SheppLogan Phantom.svg" image has been obtained by the author(s) from the Wikimedia website where it was made available by Bitic under a CC BY-SA 4.0 licence. It is included within this article on that basis. It is attributed to Larry Shepp and Benjamin F. Logan. Figure 7(m)–(r) reproduced with permission from Kundur, D & Hatzinakos, D (1998). IEEE Transactions on Signal Processing 46(2): 375–390. © Copyright 1998 IEEE.

the recovered results by DTV, IBD, NAS-RIF, TV-RIF and our proposed method, repectively. In figure 5, we consider the test images with black background degraded by different blurs without noise. From the figure, it can be seen that the performance of our proposed method is quite good since it can restore the sharp edges and avoid noise amplification. Especially, we observe from the 'Toy' image that the restored image produced by DTV is oversmooth and the resulting image by IBD still has the blur phenomenon. The restored image by NAS-RIF has some artifacts and is somewhat blurry. The resuting image by the TV-RIF method looks more clear than NAS-RIF, but has serious artifacts. Apparently, our method achieves the best visual quality among the competing methods. In figure 6, we consider the test images with nonuniform background degraded by different blurs without noise. Obviously, the artifacts are clearly more visible in the restored images by DTV, IBD, NAS-RIF and TV-RIF than the one by our proposed method on the 'letters' image. For the nonuniform background case, figure 6 shows that our proposed method can produce better restored images in visual quality and perform with PSNR values higher than those obtained by DTV, IBD, NAS-RIF and TV-RIF.

In figure 7, the test images with black background are degraded by different blurs with the noise level of BSNR = 30 dB. We compare the visual quality of the restored images by DTV,
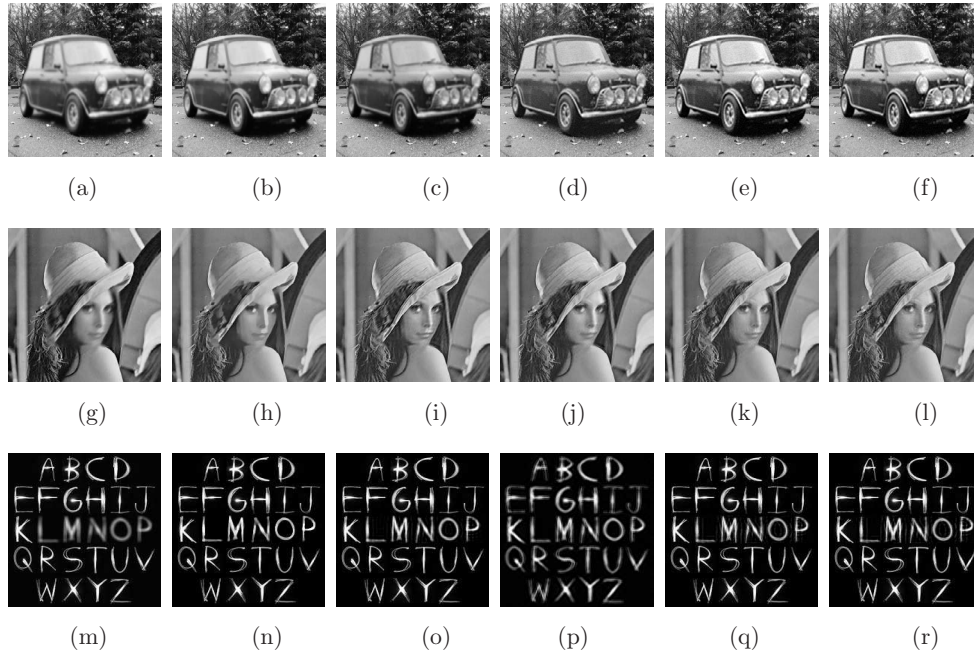
Figure 8. Comparison of results by different methods applied on blurred images with nonuniform background and noise of BSNR = 30 dB. First column: the blurred images; Second to sixth columns: the restoration results by DTV, IBD, NAS-RIF, TV-RIF and ours respectively. (a) Gaussian. (b) DTV. (c) IBD. (d) NAS-RIF. (e) TV-RIF. (f) Ours. (g) Motion. (h) DTV. (i) IBD. (j) NAS-RIF. (k) TV-RIF. (l) Ours. (m) Defocus. (n) DTV. (o) IBD. (p) NAS-RIF. (q) TV-RIF. (r) Ours. Figures 8(a)–(f) reproduced with permission from Best Car Magazine. Figures 8(g)–(l) © Playboy Enterprises, Inc. Figures 8(m)–(r) reproduced with permission from http://newgrafitimakmu.blogspot.com/2010/01/graffiti-alphabet-letter-fonts-z-light.html.

Table 3. CPU time by different methods for the 'Lena' image with different blurs.

	Blur	DTV	IBD	NAS-RIF	TV-RIF	Ours
Noise-free	Gaussian	20.1	1.5	236.5	801.2	10.0
	Motion	22.9	2.0	272.2	953.6	10.7
	Defocus	23.5	1.1	308.6	1254.6	11.4
Noisy	Gaussian	52.6	1.1	213.6	768.5	9.4
	Motion	13.4	1.4	244.2	935.1	11.9
	Defocus	125.9	1.3	284.2	1258.4	10.3

IBD, NAS-RIF, TV-RIF and our proposed method in figure 7. It is clear from the figure that the restoration results of our proposed method are visually better than those of DTV, IBD, NAS-RIF and TV-RIF. Our proposed method is able to prevent noise amplification and reduce ringing artifacts for the noisy case. In figure 8, the test images with nonuniform background are degraded by the same blurs and noise. The restoration results by the competing methods are displayed in figure 8. We see from the figure that the restored images of our proposed method look more natural. It turns out that our proposed method is quite robust to noise. Compared with DTV, IBD, NAS-RIF and TV-RIF, our proposed method appears to be very competitive with respect to visual restoration capabilities for nonuniform background.

To report the computational time, we take the 'Lena' image with size of 256×256 for example. In table 3, we give a comparison for the CPU time of DTV, IBD, NAS-RIF, TV-RIF and our proposed method under different blurs. For the original image 'Lena' degraded by the Gausssian blur in the absence of noise, our proposed method, DTV, IBD, NAS-RIF and TV-RIF need about 10.0 s, 20.1 s, 1.5 s, 236.5 s and 801.2 s respectively to estimate the blur kernel and recover the original image. The comparison clearly show that the proposed method is much faster than the DTV, NAS-RIF and TV-RIF methods. Our proposed method is more time consuming than IBD, however, this drawback is compensated by its outstanding performance. From table 3, it can be seen that we have the similar time consuming results for the noisy case on the 'Lena' image. In terms of PSNR, visual quality and CPU time, the proposed method appears to be better than the DTV, IBD, NAS-RIF and TV-RIF methods.

6. Conclusion

In this paper, we propose a new regularized inverse filtering method for blind deconvolution of images. The main idea of our method is to add two regularization terms to the objective function of NAS-RIF so as to improve the quality of blind image deconvolution. One regularization term is the TV of the resulting image obtained by convolving the inverse filter with the degraded image. The TV regularization is used to stabilize the inverse solution and alleviate sensitivity to noise. Another regularization term is the star norm of the inverse filter. We choose the star norm regularization because the inverse filter lies in a space which contains signals with large oscillations such as textures and has a small norm. The proposed minimization model is proved to be convex. We employ the first-order primal-dual method for the solution of the proposed minimization problem. In terms of PSNR, SSIM, visual quality and time consumption, numerical examples for blind image restoration are given to demonstrate that the proposed method performs better than some existing related restoration methods.

ORCID iDs

Tieyong Zeng ● https://orcid.org/0000-0002-0688-202X

References

Abdoulaev G S, Ren K and Hielscher A H 2005 Optical tomography as a pde-constrained optimization problem *Inverse Problems* **21** 1507
Aubert G and Kornprobst P 2006 *Mathematical Problems in Image Processing: Partial Differential Equations and the Calculus of Variations* vol 147 (Berlin: Springer)
Aujol J F, Aubert G, Blanc-Féraud L and Chambolle A 2005 Image decomposition into a bounded variation component and an oscillating component *J. Math. Imaging Vis.* **22** 71–88

Ayers G and Dainty J C 1988 Iterative blind deconvolution method and its applications *Opt. Lett.* **13** 547–9

Bahouri H, Chemin J Y and Danchin R 2011 *Fourier Analysis, Nonlinear Partial Differential Equations* vol 343 (Berlin: Springer)

Banham M R and Katsaggelos A K 1997 Digital image restoration *Signal Process. Mag., IEEE* **14** 24–41

Bao C, Dong B, Hou L, Shen Z, Zhang X and Zhang X 2016 Image restoration by minimizing zero norm of wavelet frame coefficients *Inverse Problems* **32** 115004

Benameur S, Mignotte M, Soucy J P and Meunier J 2008 Spect image restoration via recursive inverse filtering constrained by a probabilistic mri atlas *15th IEEE Int. Conf. on Image Processing* (IEEE) pp 2984–7

Benvenuto F, Zanella R, Zanni L and Bertero M 2009 Nonnegative least-squares image deblurring: improved gradient projection approaches *Inverse Problems* **26** 025004

Bonettini S, Zanella R and Zanni L 2008 A scaled gradient projection method for constrained image deblurring *Inverse Problems* **25** 015002

Borcea L, Callaghan T and Papanicolaou G 2013 Motion estimation and imaging of complex scenes with synthetic aperture radar *Inverse Problems* **29** 054011

Boyd S, Parikh N, Chu E, Peleato B and Eckstein J 2011 Distributed optimization and statistical learning via the alternating direction method of multipliers *Found. Trends® Mach. Learn.* **3** 1–122

Cai J F, Dong B, Osher S and Shen Z 2012a Image restoration: total variation, wavelet frames, and beyond *J. Am. Math. Soc.* **25** 1033–89

Cai J F, Ji H, Liu C and Shen Z 2012b Framelet-based blind motion deblurring from a single image *IEEE Trans. Image Process.* **21** 562–72

Calvetti D, Landi G, Reichel L and Sgallari F 2004 Non-negativity and iterative methods for ill-posed problems *Inverse Problems* **20** 1747

Campisi P and Egiazarian K 2016 *Blind Image Deconvolution: Theory and Applications* (Boca Raton, FL: CRC Press)

Chambolle A 2004 An algorithm for total variation minimization and applications *J. Math. Imaging Vis.* **20** 89–97

Chambolle A and Pock T 2011 A first-order primal-dual algorithm for convex problems with applications to imaging *J. Math. Imaging Vis.* **40** 120–45

Chan R H, Tao M and Yuan X 2013 Constrained total variation deblurring models and fast algorithms based on alternating direction method of multipliers *SIAM J. Imaging Sci.* **6** 680–97

Chan T F and Shen J J 2005 *Image Processing, Analysis: Variational, PDE, Wavelet and Stochastic Methods* (Philadelphia: SIAM)

Chan T F and Wong C K 1998 Total variation blind deconvolution *IEEE Trans. Image Process.* **7** 370–5

Chung J and Nagy J G 2010 An efficient iterative approach for large-scale separable nonlinear inverse problems *SIAM J. Sci. Comput.* **31** 4654–74

Combettes P L and Wajs V R 2005 Signal recovery by proximal forward-backward splitting *Multiscale Model. Simul.* **4** 1168–200

Ding T and Ren K 2014 Inverse transport calculations in optical imaging with subspace optimization algorithms *J. Comput. Phys.* **273** 212–26

Ding T, Ren K and Vallélian S 2015 A one-step reconstruction algorithm for quantitative photoacoustic imaging *Inverse Problems* **31** 095005

Dolui S and Michailovich O V 2011 Hybrid blind deconvolution of images using variable splitting and proximal point methods *18th IEEE Int. Conf. on Image Processing* (IEEE) pp 2709–12

Dong Y, Hintermüller M and Rincon-Camacho M M 2011 Automated regularization parameter selection in multi-scale total variation models for image restoration *J. Math. Imaging Vis.* **40** 82–104

Ekeland I and Temam R 1976 *Convex Analysis and 9 Variational Problems* (Philadelphia: SIAM)

Fornasier M, Kim Y, Langer A and Schnlieb C B 2012 Wavelet decomposition method for l2/tv-image deblurring *SIAM J. Imaging Sci.* **5** 857–85

Gerth D and Ramlau R 2014 A stochastic convergence analysis for Tikhonov regularization with sparsity constraints *Inverse Problems* **30** 055009

Goldstein T and Osher S 2009 The split Bregman method for l1-regularized problems *SIAM J. Imaging Sci.* **2** 323–43

Golub G H and Van Loan C F 2012 *Matrix Computations* vol **3** (Baltimore: Johns Hopkins University Press)

Hansen P C, Nagy J G and O'leary D P 2006 *Deblurring Images: Matrices, Spectra, and Filtering* (Philadelphia: SIAM)

Ito K and Jin B 2011 A new approach to nonlinear constrained Tikhonov regularization *Inverse Problems* **27** 105005

Jiang M and Wang G 2003 Development of blind image deconvolution and its applications *J. X-ray Sci. Technol.* **11** 13–9

Joshi N, Szeliski R and Kriegman D J 2008 PSF estimation using sharp edge prediction *IEEE Conf. on Computer Vision and Pattern Recognition* (IEEE) pp 1–8

Justen L and Ramlau R 2009 A general framework for soft-shrinkage with applications to blind deconvolution and wavelet denoising *Appl. Comput. Harmon. Anal.* **26** 43–63

Katsevich A, Silver M and Zamyatin A 2011 Local tomography and the motion estimation problem *SIAM J. Imaging Sci.* **4** 200–19

Kundur D and Hatzinakos D 1996 Blind image deconvolution *IEEE Signal Process. Mag.* **13** 43–64

Kundur D and Hatzinakos D 1998 A novel blind deconvolution scheme for image restoration using recursive filtering *IEEE Trans. Signal Process.* **46** 375–90

Li W, Li Q, Gong W and Tang S 2012 Total variation blind deconvolution employing split bregman iteration *J. Vis. Commun. Image Represent.* **23** 409–17

Likas A C and Galatsanos N P 2004 A variational approach for bayesian blind image deconvolution *IEEE Trans. Signal Process.* **52** 2222–33

Lou Y, Esser E, Zhao H and Xin J 2014 Partially blind deblurring of barcode from out-of-focus blur *SIAM J. Imaging Sci.* **7** 740–60

Louis A 1999 A unified approach to regularization methods for linear ill-posed problems *Inverse Problems* **15** 489

Lv X G, Huang T Z and Ren Z G 2009 A modified T Chan's preconditioner for Toeplitz systems *Comput. Math. Appl.* **58** 693–9

Lv X G, Huang T Z, Xu Z B and Zhao X L 2012 Kronecker product approximations for image restoration with whole-sample symmetric boundary conditions *Inf. Sci.* **186** 150–63

Ma L, Ng M, Yu J and Zeng T 2013 Efficient box-constrained tv-type-l1 algorithms for restoring images with impulse noise *J. Comput. Math.* **31** 249–70

Matsuyama M, Tanji Y and Tanaka M 2000 Enhancing the ability of nas-rif algorithm for blind image deconvolution *Proc. IEEE Int. Symp. on Circuits and Systems 2000 (Geneva)* vol 4 (IEEE) pp 553–6

McCallum B 1990 Blind deconvolution by simulated annealing *Opt. Commun.* **75** 101–5

Meyer Y 2001 *Oscillating Patterns in Image Processing, Nonlinear Evolution Equations: the Fifteenth Dean Jacqueline B. Lewis Memorial Lectures* vol 22 (Providence, RI: American Mathematical Society)

Michailovich O and Tannenbaum A 2007 Blind deconvolution of medical ultrasound images: a parametric inverse filtering approach *IEEE Trans. Image Process.* **16** 3005–19

Molina R and Ripley B 1993 Using spatial models as priors in astronomical image analysis *J. Appl. Stat.* **20** 281–98

Ng M K 2004 *Iterative Methods for Toeplitz Systems* (Oxford: Oxford University Press)

Ng M K, Chan R H and Tang W C 1999 A fast algorithm for deblurring models with neumann boundary conditions *SIAM J. Sci. Comput.* **21** 851–66

Ng M K, Plemmons R J and Qiao S 2000 Regularization of rif blind image deconvolution *IEEE Trans. Image Process.* **9** 1130–4

Ong C A and Chambers J A 1999 An enhanced nas-rif algorithm for blind image deconvolution *IEEE Trans. Image Process.* **8** 988–92

Ouyang Y, Chen Y, Lan G and Pasiliao E Jr 2015 An accelerated linearized alternating direction method of multipliers *SIAM J. Imaging Sci.* **8** 644–81

Paragios N, Chen Y and Faugeras O D 2006 *Handbook of Mathematical Models in Computer Vision* (Berlin: Springer)

Pöschl C and Scherzer O 2015 Exact solutions of one-dimensional total generalized variation *Commun. Math. Sci.* **13** 171–202

Pratt W K 2013 *Introduction to Digital Image Processing* (Boca Raton, FL: CRC Press)

Rudin L I, Osher S and Fatemi E 1992 Nonlinear total variation based noise removal algorithms *Physica* D **60** 259–68

Sherman J and Morrison W J 1950 Adjustment of an inverse matrix corresponding to a change in one element of a given matrix *Ann. Math. Stat.* **21** 124–7

Tikhonov A N and Arsenin V Y 1977 *Solution of Ill-Posed Problems* (Washington DC: Winston & Sons)

Vese L 2001 A study in the bv space of a denoising–deblurring variational problem *Appl. Math. Optim.* **44** 131–61

Vese L A and Osher S J 2003 Modeling textures with total variation minimization and oscillating patterns in image processing *J. Sci. Comput.* **19** 553–72

Vogel C R 2002 *Computational Methods for Inverse Problems* vol 23 (Philadelphia: SIAM)

Wang W and Ng M K 2016 Convex regularized inverse filtering methods for blind image deconvolution *Signal, Image Video Process.* **10** 1353–60

Wang Z, Bovik A C, Sheikh H R and Simoncelli E P 2004 Image quality assessment: from error visibility to structural similarity *IEEE Trans. Image Process.* **13** 600–12

Wu C and Tai X C 2010 Augmented lagrangian method, dual methods, and split bregman iteration for rof, vectorial tv, and high order models *SIAM J. Imaging Sci.* **3** 300–39

Xu L and Jia J 2010 Two-phase kernel estimation for robust motion deblurring *European Conf. Computer Vision* (Berlin: Springer) pp 157–70

Zhang Z 1997 Parameter estimation techniques: a tutorial with application to conic fitting *Image Vis. Comput.* **15** 59–76

Zunino A, Benvenuto F, Armadillo E, Bertero M and Bozzo E 2009 Iterative deconvolution and semiblind deconvolution methods in magnetic archaeological prospecting *Geophysics* **74** 43–51